

Article

## Mechanisms of Charge Transport through Monolayer-Modified Polycrystalline Gold Electrodes in the Absence of Redox-Active Moieties

Chaitanya Gupta, Mark A. Shannon, and Paul J. A. Kenis

*J. Phys. Chem. C*, **2009**, 113 (11), 4687-4705 • DOI: 10.1021/jp8090045 • Publication Date (Web): 20 February 2009

Downloaded from <http://pubs.acs.org> on March 12, 2009

### More About This Article

Additional resources and features associated with this article are available within the HTML version:

- Supporting Information
- Access to high resolution figures
- Links to articles and content related to this article
- Copyright permission to reproduce figures and/or text from this article

[View the Full Text HTML](#)

# Mechanisms of Charge Transport through Monolayer-Modified Polycrystalline Gold Electrodes in the Absence of Redox-Active Moieties

Chaitanya Gupta,<sup>†</sup> Mark A. Shannon,<sup>\*,†,‡,§</sup> and Paul J. A. Kenis<sup>\*,†,‡,§</sup>

Department of Chemical & Biomolecular Engineering, University of Illinois at Urbana–Champaign, Urbana, Illinois 61801, Department of Mechanical Science & Engineering, University of Illinois at Urbana–Champaign, Urbana, Illinois 61801, Beckman Institute for Advanced Science and Technology, University of Illinois at Urbana–Champaign, Urbana, Illinois 61801

Received: October 10, 2008; Revised Manuscript Received: December 23, 2008

The charge transport processes in thin insulating films separating a gold electrode and an electrolyte solution are characterized using a constitutive admittance expression that accounts for conduction, diffusion, and polarization of charge within the films. We specifically investigate cases in which the electrolyte solution does not contain electroactive ions. The general impedance response of all gold–monolayer–electrolyte systems to an applied potential, for systems in which the electrolyte does not contain any redox-active species, suggests the existence of a potential regime where the current is limited by the rate of charge transport through the monolayer phase and a regime limited by the rate of charge transfer at the monolayer–electrolyte interface. The monolayer free charge density that appears as a parameter in the admittance expression is evaluated from the measured admittance in both regimes. This calculated parameter describes two field-dependent mechanisms of charge transport in the monolayer phase, for potentials where charge transport limits the flow of charge through the insulating films. These charge transport mechanisms follow well-characterized solid-state mechanistic models of charge conduction; namely, Ohmic conduction at low electric fields and space–charge-limited transport at higher electric fields. Quantum mechanical tunneling effects are also observed at large ( $\sim 10^9$  V/m) electric fields in the monolayer. For potential regimes in which the charge transfer is rate-limiting, the evaluation of the monolayer free charge density from the impedance response results in current densities that are described by the thermal activation of reacting species over a free energy barrier at the monolayer–electrolyte interface. At low electric fields, the rate-limiting process involves the thermally activated reorganization of the solvent molecules, in accordance with the Marcus theory, and for higher fields, the observed current is limited by the thermal hopping of transferring electrons over an electrostatic potential energy barrier within the monolayer phase. The charge transport and charge transfer mechanisms are also shown to be dependent on physical and chemical interactions between the monolayer functional group and the electrolyte constituents at the Stern layer. These interactions are described using empirical parameters obtained from the mechanistic expressions for these charge transport and transfer processes, and the effect of varying electrolyte properties on these parameters is examined in detail here.

## Introduction

Solid electrode surfaces modified by self-assembled monolayers have been used extensively to investigate the effects of monolayer film thickness and functional end groups on electron transfer, since these molecules can form structured, homogeneous assemblies with well-defined film thickness and interfacial properties.<sup>1–6</sup> Electron transfer events at  $\omega$ -functionalized monolayers adsorbed on gold substrates have been studied in detail for cases in which the electron donating/accepting redox-active species is dissolved in the electrolyte<sup>7,8</sup> as well as for situations when the redox-active species constitutes the functional end group in the alkyl chain.<sup>1,3,9–13</sup> Initial attempts at describing the current overpotential curves for these cases relied on the assumption that the exchange of charge between the metal phase and the redox-active species is an adiabatic process and that tunneling of charge through the monolayer film did not play a significant role in the reaction kinetics.<sup>1,4</sup> Subsequently, the

adiabatic charge transfer theory was modified to account for the tunneling of electrons through the monolayer film. The tunneling process was, however, modeled on Schmickler's description of adiabatic resonance tunneling within iron oxide thin films<sup>14,15</sup> in which the charge was assumed to tunnel across a rectangular potential energy barrier from a donor to an acceptor state.<sup>16</sup> A more complete description of the charge transfer between a metallic electrode and a redox-active moiety that are separated by an intervening monolayer film involves a chemical kinetics approach to defining a bridge-mediated reaction between an electron donor and an acceptor species.<sup>4,13,17</sup> The underlying redox reaction proceeds directly via a nonadiabatic molecular orbital interaction between the reacting species in the electrolyte and the metal electrode. The effect of the intervening monolayer film is introduced as a quantum mechanical coupling factor between the metal electrode and the electrolyte species, commonly referred to as the transfer integral, in the expression for the rate constant.<sup>17,18</sup> The formulation of the coupling factor usually requires a description of the electronic structure of the molecular bridge, and the accuracy of the derived rate expression is a strong function of the electronic structural model adopted

\* Corresponding authors. E-mails: mshannon@uiuc.edu, kenis@uiuc.edu.

<sup>†</sup> Department of Chemical & Biomolecular Engineering.

<sup>‡</sup> Department of Mechanical Science & Engineering.

<sup>§</sup> Beckman Institute for Advanced Science and Technology.

for this calculation.<sup>19,20</sup> Although these quantum mechanical descriptions of charge transport through the monolayer film refer directly to the nuclear and electronic factors that affect the mechanism of charge conduction through the monolayer film, the ease with which these results can be interpreted and compared to experimental data decreases rapidly with increasing complexity in the calculations for the transfer integral.<sup>19</sup> However, since the calculated transfer integral decreases exponentially with monolayer film thickness,<sup>20</sup> this simple functional dependence between the rate constant and the monolayer chain length has been studied extensively and is, in our understanding, the most commonly investigated experimental parameter in these donor–bridge–acceptor systems.<sup>21,22</sup> A comparison between the experimentally obtained decay constant and the *ab initio* decay constants calculated from the transfer integral suggests that the primary mechanism of charge transport through the monolayer film is tunneling through  $\sigma$ -bonds,<sup>16,21</sup> and that a small amount of charge is also transported by a process of electron hopping between alkane chains in the monolayer film.<sup>21</sup>

These quantum mechanical models of charge transport within an alkane thiol monolayer film are limited to specific cases in which a redox-active moiety is either dissolved in the electrolyte or is tethered to the end of the monolayer chain and this electroactive species acts as the donor or acceptor species for the transported electron. As expected, these studies indicated that background electrolyte anions play an insignificant role in the electron transfer kinetics of a gold–monolayer–electrolyte system, since the exchange of electrons between the metal phase and the electrolyte solutions is dominated by the electronic interaction between the electroactive ion and the metal phase.<sup>4</sup> Consequently, background electrolyte properties such as pH have a small impact on the observed results, and the effect of varying these parameters is limited to shifts induced in the formal potential for the electroactive species. Moreover, the use of redox-active species in the electrolyte also restricts the range of applied potentials, since significantly large anodic or cathodic potentials result in the onset of a mass transfer limitation in which the charge transport through the monolayer phase is no longer rate-limiting. The mass transfer limit, manifested by a Warburg-like impedance characteristic,<sup>6</sup> masks the effect of the monolayer film and the monolayer–electrolyte interface on the observed current density at these large anodic and cathodic potentials. Thus, by using electrolyte-dissolved, redox-active species to probe charge transfer at monolayer-modified electrodes, additional information about the physicochemical properties of the electrode–electrolyte interface is lost, as we demonstrate in this paper. In addition, most experimental work on charge transfer at monolayer-modified electrodes relies on the use of the simpler adiabatic charge transfer theory to explain observed kinetic data and is at odds with conventional understanding that describes the electron transfer event as nonadiabatic. Accordingly, the kinetic rate constant has a Tafel-like functional dependence on the potential bias applied to the metallic phase in accordance with the adiabatic description of electron exchange between the metal and the redox-active species,<sup>1,16</sup> where the anisotropy between the cathodic and anodic arms of the Tafel plots was attributed to the potential-dependent tunneling of charge through the alkane backbone of the monolayer film.<sup>16</sup> However, when these bridge electron transfer reactions are described as nonadiabatic electronic interactions between the donor and the acceptor species, the mechanism by which the potential bias affects the observed rate

constant is difficult to identify because of the complexity of the calculated transfer integral.

These problems are alleviated to a certain extent in the gold–monolayer–electrolyte experimental systems investigated here, in which the electrolyte contains no electroactive species. The observed current density in these systems has been characterized in the literature as leakage current that occurs due to the penetration of electrolyte ions within pinhole defects in the monolayer film.<sup>23–25</sup> Since there is no electroactive moiety acting as the dominant electron donor or acceptor molecule, the effect of background electrolyte properties on this observed current density is expected to become significant in these situations, and the electronic coupling between the electrolyte constituents and the metal can provide valuable information on the state of the monolayer–electrolyte interface, as we show in this paper and elsewhere.<sup>26</sup> The leakage current is also a strong function of the applied potential,<sup>24,27</sup> and in this paper, we demonstrate a methodology that uses this dependence of current on applied potential to describe the nonadiabatic mechanisms of charge transport within thin monolayer films without resorting to the use of quantum mechanical transfer integrals that often need unknown parameters to evaluate. We use empirical parameters derived from these mechanistic descriptions of charge transport to evaluate the physicochemical properties of the monolayer–electrolyte interface. In the absence of electrochemically active ions, the electron-donating or accepting states in the electrolyte are, expectedly, the hydroxyl or proton ions in the aqueous electrolyte. Consequently, the system does not suffer from mass transfer limitations at large anodic or cathodic potentials, thereby providing a larger potential range for examination. To our knowledge, a quantitative mechanistic description of current–potential behavior in monolayer films for the case when the electrolyte has no electroactive species is still lacking.

Impedance spectroscopy has been used extensively to investigate charge transfer at monolayer–electrolyte interfaces, for cases when the electrolyte may<sup>28–31</sup> or may not<sup>23–25,27,32</sup> contain a redox-active ion. The low-frequency impedance response of a gold–monolayer–electrolyte system to applied potential, for the case when the electrolyte has no electroactive ions, yields three distinct regimes defined by the magnitude of the applied potential, as discussed in reference 26: (a) a purely capacitive regime at anodic potentials, (b) a predominantly resistive regime for cathodic potentials,<sup>24,32</sup> and (c) a capacitive response with a statistically significant real component at large anodic potentials. As discussed before, we could not find any referrals to regime c in the literature. At anodic potentials, small deviations from ideal capacitive behavior were attributed to leakage current due to ion penetration through pinhole defects in the monolayer films due to imperfect self-assembly or because of defects on the polycrystalline gold substrate.<sup>23</sup> The resistive behavior at large cathodic potentials was hypothesized to be due to an increase in the size of these pinhole structures when the applied potential increases beyond a certain critical threshold ( $V_c$ ).<sup>25</sup> However, this hypothesis was based on the application of multiple empirically constructed circuit models to the cathodic potential regime of the impedance response, and the interpretation of the potential behavior was based on the goodness-of-fit of the phenomenological circuits to the impedance response in this potential regime. Hitherto now, the *reason* for the existence of a threshold potential and the mechanism for an increase in the size of pinhole defects at applied voltages more cathodic than the critical potential remain unexplained. Similarly, the hypothesis that charge transport through a monolayer film occurs due

to ion penetration in pinhole defects remains a qualitative assertion justified by an empirical linear circuit model that lacks a detailed explanation of how the ion traverses the pinhole structure and subsequently exchanges charge with the gold substrate. Therefore, a quantitative description of how the leakage current varies as a function of the applied potential over the entire potential range is required to identify the mechanism(s) of charge transport within the monolayer film. Moreover, an explanation of the nonlinear transition between anodic and cathodic potential regime leads to a better understanding of how a monolayer-modified electrode can exhibit a response that varies continuously from purely capacitive to purely resistive over the entire potential spectrum.

As a means to help answer these questions, a method to analyze the real and imaginary components of the impedance of a gold–monolayer–electrolyte system was developed in reference 26, where the constitutive equation for charge transport was modified to yield an expression for the system admittance or the reciprocal impedance. At low frequencies, the conduction and diffusion current densities contribute to the real part of the admittance, and the imaginary component has been shown to be a function of the displacement current density. Thus, the values of the electric field and the injected free charge density in the monolayer film as functions of the applied voltage can be extracted from a potential-based spectrum of the admittance of a specific gold–monolayer–electrolyte system. We illustrated a generic analogy between a solid-state Schottky diode and the gold–monolayer–electrolyte system, as well as the existence of physicochemical parameters such as the built-in electric field, equilibrium potential, and the potential of zero field (PZF). The characterization of the properties of specific monolayer–electrolyte interfaces with the help of these parameters was also discussed. Although the technique that was introduced is applicable to the analysis of the admittance of a gold–monolayer–electrolyte system over the entire potential range, we restricted the discussion to the values of the electric field at two specific potentials; namely, at zero applied voltage and at the potential where the net current density is zero. The measured electric fields at these specific points in the potential spectrum correspond to intrinsic properties of the monolayer–electrolyte interface that are independent of applied potential, as was demonstrated in detail in reference 26.

In this paper, we extend the analysis to consider the current potential behavior of different gold–monolayer–electrolyte systems over the entire potential regime, from strongly anodic to strongly cathodic, but well within the regime of electrochemical stability for the gold–thiol bond. Here, “anodic” and “cathodic” potentials are measured with respect to the PZF. We broadly identify the different potential regimes in which charge transport through the monolayer film, or charge transfer at the monolayer–electrolyte interface, is rate-limiting. Accordingly, the potential dependent expressions for charge conduction and diffusion are described for these different potential regimes using the admittance methodology detailed in reference 26. The conduction and diffusion current densities thus obtained are compared with multiple solid-state mechanisms of charge transport, and the assumptions underlying the applicability of these solid-state models to charge transport in a gold–monolayer–electrolyte system are also examined in depth. These mechanistic descriptions of charge transport and charge transfer, when fit to the observed current–potential characteristics of a gold–monolayer–electrolyte system, yield empirical parameters that are then used to describe the physical and chemical properties of the monolayer–electrolyte interface. The schematic in Figure

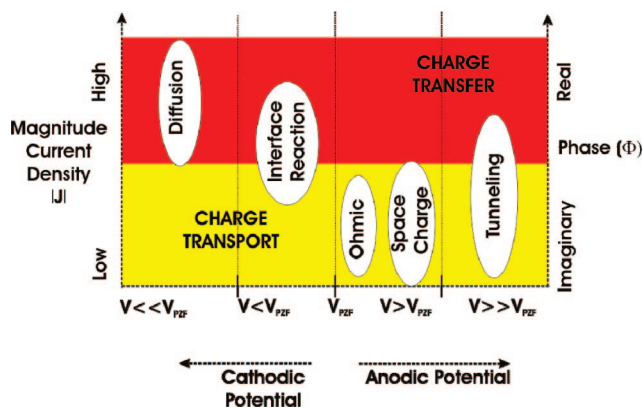


**Figure 1.** Schematic illustrating multiple charge transport and charge transfer mechanisms for different potential regimes. The effect on the magnitude of current density and the low frequency phase is also depicted.

1 summarizes the different charge transport and charge transfer mechanisms as functions of the applied potential. Also depicted is the effect on the observed current density and low frequency phase when the specific mechanism is rate-limiting. For anodic potentials, the conduction current density dominates over the diffusion contribution, and we show that the functional dependence of the conduction current density on the electric field in the monolayer follows Ohm’s law at low electric fields, and for larger electric fields, the current density becomes space–charge-limited (see the Results and Discussion, section i). On the application of very large electric fields, the net current density is observed to be limited by the quantum mechanical tunneling of electrons from the ground-state energy level of the immobilized ions at the Stern layer through the monolayer conduction band and into empty states in the bulk metal (see the Results and Discussion, section ii). For the cathodic potential regime, on the other hand, the diffusion current density exceeds the contribution due to the conduction mechanism. The functional dependence of the diffusion current on the applied potential corresponds to the thermal activation of the reactant species over a free energy barrier. We demonstrate that for small deviations from the PZF, the thermal activation of the solvent polarization limits the charge transfer process (see the Results and Discussion, section iv), whereas for larger cathodic potentials, the process of electrons thermally hopping over an electrostatic potential energy barrier is the rate-limiting mechanism (see the Results and Discussion, section iii).

## Theory

The objective of the experiments is to determine the mechanisms of charge transport through a monolayer on metal that is in contact with an electrolyte using only the observables of voltage and current, both as functions of time. From the current, voltage, and phase between them, we seek to deduce the charge transport and charge transfer barriers at each point in the metal–monolayer–electrolyte system, including the interfaces as well as the governing mechanisms spatially within the system, including the effect of heterogeneous charge transport structures, such as pinholes. In this section, we will present the time-varying electrical impedance admittance model that accounts for capacitive charge storage along with leakage, with particular attention to the effect of pinholes and charge transfer barriers. Due to the importance of conduction from the metal to the monolayer on the overall charge transport mechanisms in the monolayer and to the electrolyte, we also present a detailed analysis of the Ohmic nature of the electrical contact at the metal–monolayer interface.

**Charge Transport and Charge Transfer Barriers.** The gold–monolayer–electrolyte system is modeled as a current-leaking parallel plate capacitor, in which the metal–monolayer interface and the monolayer–electrolyte interface constitute the two plates of the capacitor between which the charge is transported. Although each interface is associated with a finite thickness, the length of the alkane backbone in the monolayer phase exceeds the width of each interface by at least an order of magnitude, and therefore, the plates of the capacitor bounding the dielectric medium of the monolayer phase can be considered as infinitesimally thin. The application of a potential bias to the gold surface with respect to a reference electrode in the bulk electrolyte solution results in a potential drop of magnitude  $\varphi_M - \varphi_{\text{OHP}}$  across the capacitor system, where  $\varphi_M$  is the applied potential at the surface of the metal and  $\varphi_{\text{OHP}}$  is the electrostatic potential at the outer Helmholtz plane. The resulting steady-state flow of charge through the gold–monolayer–electrolyte system due to the applied potential is a transport process that is limited in rate by the slowest step, and the nature of the rate-limiting process in the charge transport process depends on the structure of the thiol monolayer film. Thus, a key question that needs to be considered in the study of charge transport through gold–monolayer–electrolyte systems is the effect of monolayer pinhole defects on current leakage. Two limiting cases are considered here in this context: a monolayer film with (a) “small” and (b) “large” pinhole defects, where the terms “small” and “large” are defined below.

A self-assembled monolayer film with pinhole defects of sufficiently small pore diameter does not allow for the intake of solvent molecules and limits the intake of dehydrated ionic species within the pinhole structure as well, since there is a considerable enthalpy barrier for an ion to lose the hydration shell before entering the defect pore. Consequently, there is a large transport barrier that obstructs the transport of the dehydrated ion in the small pinhole defect from the monolayer–electrolyte interface to the metal–monolayer interface. In addition, there is a free energy barrier to the exchange of an electron between the electronic continuum of the metal phase and the energy levels of the dehydrated ionic species at the metal–monolayer interface. This barrier alone would be on the order of the work function for gold ( $\sim 5.4$  eV). Since the current begins to increase significantly for much lower potentials ( $< 1$  eV),<sup>26</sup> this mechanism of charge transport is negligible. The current in these ideal monolayer films is, instead, limited by one of three foreseeable barriers: (a) a free energy barrier at the monolayer–electrolyte interface for the exchange of electrons between the monolayer functional group and the energy levels of the partially dehydrated ions immobilized at the Stern layer, (b) a transport barrier that limits the rate of transport of the electron in the alkane structure and (c) a free energy barrier at the gold–monolayer interface that inhibits electron exchange between the metal and the alkane phase.

An alkane thiol monolayer film with large pinhole defects that is substantially penetrated by the hydrated ions and free solvent molecules, on the other hand, is limited either by the movement of ions through the defect structure or by the flow of electrons across the alkane structure. The two charge flow mechanisms are equally probable, and there is no a priori information that allows us to discount one mechanism in favor of the other. Each charge flow path is associated with a sequence of energy barriers that inhibit this flow, as discussed above.<sup>26</sup> As the ions move through the pinhole defects under the influence of the applied electric field and driving concentration gradients, they experience a transport barrier that limits the migration rate

through the defect pore. The ions also encounter a free energy barrier to the transfer of charge to the exposed gold atoms at the metal–electrolyte interface. However, there is no corresponding free energy barrier to charge transfer at the monolayer–electrolyte interface for this charge flow path, since the assumption here is that the ions penetrate the large pores with their hydration spheres intact. Analogous to the case for small pinhole defects, the path of charge flow determined by the migration of electrons through the alkane structure is limited by one of the three barriers discussed above. An impedance measurement for a gold–monolayer–electrolyte system limited by one of these two possible processes (namely, the migration of ions through the pinhole defects or the movement of electrons via the alkane backbone of the monolayer film) quantitatively characterizes the nature of the largest barrier to the flow of charge in this system.

Low-frequency phase information in the impedance measurement is a useful guide in determining whether charge transport/migration through a medium or charge transfer at a particular interface is rate-limiting. The implications of low frequency impedance phase data are better understood by comparing the qualitative response of the experimental gold–monolayer–electrolyte system to that of a solid-state parallel plate capacitor. As discussed above, a gold–monolayer–electrolyte system behaves like a leaking parallel plate capacitor that stores charge at the Stern layer and also allows for charge flow across the dielectric film, either through pinhole defects or by electron transport across the alkane structure. A solid-state capacitor that exhibits a small amount of leakage current at steady state has a low-frequency phase response slightly greater than  $-90^\circ$  and is considered almost ideal. Thick dielectric films tend to behave like these “almost ideal” capacitors, since the transport of charge at steady state across the medium is limited by the large path length that the charge has to traverse. Therefore, the observed steady-state current density for these thick dielectric films is limited by the transport barrier to charge flow. By analogy, current density and impedance values, in the potential regimes where the low frequency impedance response of the gold–monolayer–electrolyte system approaches  $90^\circ$ , quantitatively describe features related to the transport barrier in the monolayer film (Figure 2a). However, in the other limit, when the thickness of the dielectric medium between the plates of the solid-state parallel plate capacitor becomes infinitesimally small, charge transport between the closely spaced plates is no longer rate-limiting. Instead, the observed steady state current density in this hypothetical system is characterized by the contact resistance between the two plates. By direct analogy, the potential regime in which the experimental gold–monolayer–electrolyte system exhibits a resistive behavior at low frequencies describes a system limited by the barrier to charge transfer at the relevant interface (Figure 2b).

A reasonably smooth polycrystalline gold surface is used in the following experiments to minimize the frequency of pinhole defects in the film, and the roughness in the substrate was characterized by a series of electrochemical surface area measurements as reported in reference 25. However, the presence of pinholes in the monolayer film cannot be ruled out definitively.<sup>33</sup> Since the exact mechanism for charge transport (i.e., ion migration or electron transport) is unclear from available information prior to the experiment, a method of analyzing the gold–monolayer–electrolyte impedance that is applicable to any description of the transport process was developed.<sup>26</sup> The equation for charge transport, which can describe both ion migration and electron transport, was dif-

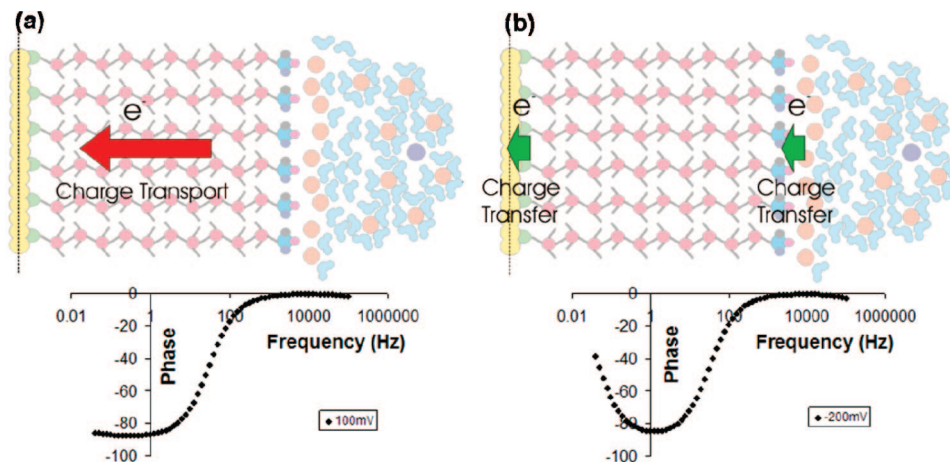


**Figure 2.** Schematic illustrating the phase behavior in the impedance response of a gold–monolayer–electrolyte system to applied potential for (a) a charge-transport-limited system and (b) a system limited by the charge transfer barrier either at the gold–monolayer or the monolayer–electrolyte interfaces.

ferentiated with respect to the applied potential to yield a constitutive expression for the low frequency admittance,  $Y_{\text{sys}}$ , of a gold–monolayer–electrolyte system such that

$$Y_{\text{sys}}(\omega) = Y_{\text{sys}}^{\text{Re}} + iY_{\text{sys}}^{\text{Im}} = \frac{\partial J(\omega)}{\partial \varphi_M} = \frac{\partial}{\partial \varphi_M} \left( \mu \rho E - D \frac{\partial \rho}{\partial x} \right) + i\omega \frac{\partial}{\partial \varphi_M} (\varepsilon_M E) \quad (1)$$

where  $\varepsilon_M$  is the low-frequency dielectric permittivity of the monolayer phase. The real and imaginary components of the admittance are extracted from the modified charge transport expression integrated with respect to the applied potential, and the resulting expressions are fit to the corresponding experimentally observed quantities to give the free charge density ( $\rho$ ) and electric field within the monolayer film ( $E$ ). The evaluation of these quantities rests on the determination of the charge mobility ( $\mu$ ) and diffusivity ( $D$ ) within the monolayer film. These transport parameters are estimated from

$$D \sim \frac{J_0 \beta^2}{\varepsilon E_0} \quad (2a)$$

and

$$\mu \sim \frac{J_0 \beta}{\varepsilon E_0^2} \quad (2b)$$

These relations are derived from a scaling argument, detailed in reference 26, that does not appeal to a specific mechanism of charge transport within the monolayer film. The electric field, evaluated from the imaginary component of eq 1, is the average electric field, and we have demonstrated the equivalence between the average and local electric field because of the finite charge size assumption.<sup>26</sup> Due to this equivalence, the electric field described by eq 1 is independent of any assumptions on the nature of the transport mechanism.

Therefore, to demonstrate that ion migration through pinhole defects has a negligible contribution to the observed current density, we described the dependence of the built-in electric field and the equilibrium electric field on the electrolyte properties and functional end group chemistry.<sup>26</sup> Both the built-in and equilibrium electric fields increase with increasing electronegativity of the monolayer end group, whereas for large pinholes, these two parameters are expected to be weakly

decreasing functions of the end group electronegativity.<sup>26</sup> Additionally, the linear dependence of the two parameters on the bulk electrolyte properties, such as pH and concentration, indicates that there is equilibrium between the charge transfer barrier, characterized by built-in field and equilibrium field, and the bulk electrolyte solution. We reasoned that equilibrium between the charge transfer barrier and the bulk electrolyte is possible only if the charge transfer barrier is located at the monolayer–electrolyte interface, which rules out ion transport through pinholes as a mechanism for charge transport.<sup>26</sup> In addition, we obtained the low-field conductivity of the monolayer film from the estimate for charge mobility ( $\mu$ ) in eq 2b and demonstrated agreement with reported low-field conductivity of organic thin films, indicating that electron flow along the alkane structure, and not ion transport, is the dominant mechanism for charge transport.<sup>26</sup>

The calculation of  $\rho$ , on the other hand, requires the specification of an interface charge density as a boundary condition, for which the mechanism of charge transport must be specified. The flow of charge is limited by one of three barriers described above, since electron transport is the most probable mechanism for charge transport in the gold–monolayer–electrolyte system, where the metal–monolayer barrier was assumed to be negligible as compared to the charge transfer barrier at the monolayer–electrolyte interface.<sup>26</sup> This assumption, in turn, facilitates the specification of the metal–monolayer surface charge density. The section below reexamines the underlying assumption of negligible charge transfer resistance at a metal–monolayer interface, which is central to the calculation of the free charge density.

**Ohmic Nature of the Electrical Contact at the Metal–monolayer Interface.** One of the three free energy barriers to the charge flow process through the alkane structure of a monolayer film is the electrostatic energy barrier for electron exchange between the gold Fermi level and the LUMO of the monolayer phase, as discussed above. We proposed that this barrier is negligible in comparison to the transport barrier in the alkane phase and the charge exchange energy barrier at the monolayer–electrolyte interface. A qualitative justification was advanced to support this assertion in reference 26. The polarization induced in the monolayer film due to the surface charge density at the Stern layer and the charged diffuse layer reduces the effective barrier height that exists at the gold–monolayer interface. We give support to this hypothesis below with the

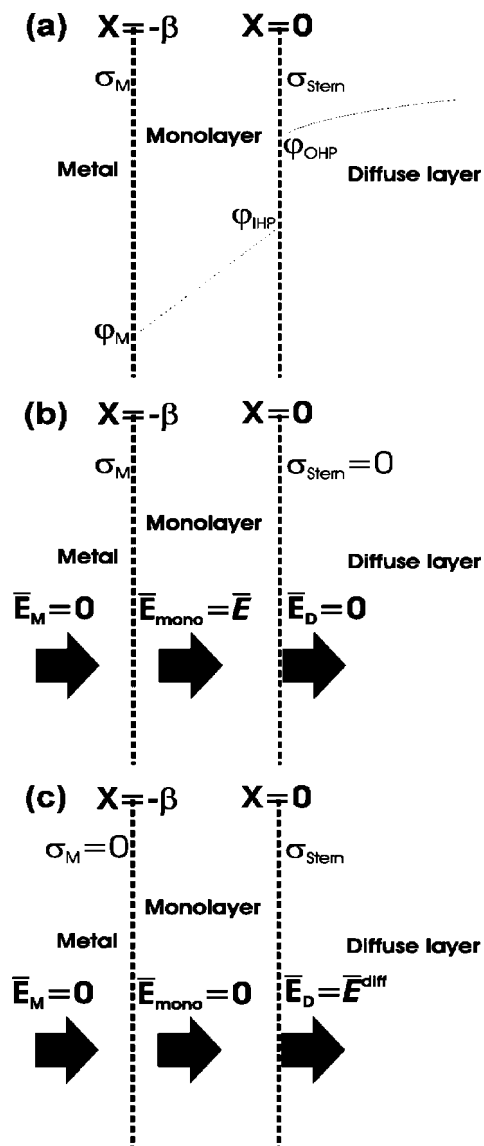


**Figure 3.** (a) Electrostatic model for the gold–monolayer–electrolyte system. Calculation of polarization fields due to (b) metal–monolayer and (c) monolayer–electrolyte surface charge densities involves the independent solution of two electrostatic problems with appropriate Neumann boundary conditions that can be linearly superposed to get the original system in part a.

aid of the leaky capacitor model of the gold–monolayer–electrolyte system introduced previously (Figure 3a).

The effect of induced polarization on the gold–monolayer interface barrier is determined by the microscopic electric field experienced by an electron at that location. For a continuous dielectric medium, this field is given by<sup>34</sup>

$$\bar{E}_{\text{micro}}(x) = \bar{E}(x) + \bar{E}^{\text{near}}(x) - \bar{E}_{\text{macro}}^{\text{near}}(x) \quad (3)$$

Here,  $\bar{E}(x)$  is the averaged macroscopic field or the observed field, and  $\bar{E}^{\text{near}}(x)$  and  $\bar{E}_{\text{macro}}^{\text{near}}(x)$  are the microscopic and macroscopic contributions to the electric field from the immediate neighborhood of the point  $x$  at the gold–monolayer interface where the electric field is evaluated. The size of the neighborhood that defines the “near” region ( $r$ ) in eq 2a is much smaller than the characteristic wavelength of the macroscopic fields ( $\lambda_M$ ) but is much larger than the molecular dimension of the system  $a$ ; that is,  $\lambda_M \gg r \gg a$ .<sup>35</sup> Since the monolayer film consists of only a few methylene units in width, both the charge

densities at the metal–monolayer and monolayer–electrolyte interface contribute to the nearfield component of the macroscopic electric field through the resulting polarization densities in the alkane structure. Thus, for a planar geometric configuration, as depicted by the capacitor model, the macroscopic contribution to the electric field at the gold–monolayer interface from the immediate neighborhood is given by<sup>36,37</sup>

$$\bar{E}_{\text{macro}}^{\text{near}}(x) = \frac{-\bar{P}_M(x) - \bar{P}_E(x)}{\epsilon_0} \quad (4)$$

where  $\bar{P}_M(x)$  and  $\bar{P}_E(x)$  are the polarization densities induced by the surface charge at the gold–monolayer interface and the monolayer–electrolyte interface respectively, and  $\epsilon_0$  is the dielectric permittivity of vacuum. The microscopic contribution to the electric field from the neighboring medium is negligible, by symmetry arguments, for the case when the dielectric has a semicrystalline structure, and therefore,  $\bar{E}^{\text{near}}(x) = 0$ .<sup>36</sup> The polarization due to the metal surface charge is evaluated from the application of Gauss’s law to the thin film electrostatic model in Figure 3b, where the finite charge size assumption<sup>26</sup> for the thin film structure gives

$$\bar{E}(x) = \frac{\sigma_M}{\epsilon_M} = -\frac{\bar{P}_M}{\epsilon_0} \quad (5)$$

Here,  $\sigma_M$  is the surface charge density at the metal–monolayer. Therefore, substituting eqs 4 and 5 in 3 yields

$$\bar{E}_{\text{micro}}^{\text{monolayer}}(x) = \frac{\bar{P}_E(x)}{\epsilon_0} \quad (6)$$

The microscopic electric field calculated from eq 6 applies to the continuous alkane phase of the dielectric medium. However, the alkane backbone of the monolayer film is linked to the gold-bonded thiol moiety at the gold–monolayer interface and to the functional group centered on the inner Helmholtz plane. Therefore, an electron at these locations experiences not just the local electric field due to the polarized dielectric medium as evaluated from eq 6 but also the microscopic field that results due to the phases adjacent to the alkane backbone; namely, the gold electrode and the Stern layer, respectively. In either case, the microscopic contribution due to the neighboring phases is described by eq 3, where the  $\bar{E}_{\text{macro}}^{\text{near}}(x)$  component that exists due to charges or polarization density in the immediate vicinity of  $x$  would be negligible, since both the metal phase and the medium between the inner and outer Helmholtz planes contain negligible free and bound charge density. Thus, we have

$$\bar{E}_{\text{micro}}^{\text{metal}}(x) = \bar{E}(x) \quad (7a)$$

and

$$\bar{E}_{\text{micro}}^{\text{Stern}}(x) = \bar{E}(x) \quad (7b)$$

The contribution due to the polarization induced by the Stern layer surface charge density is already accounted for in eq 6 and, therefore, is not considered in the evaluation of the microscopic electric field for the Stern layer ( $\bar{E}_{\text{micro}}^{\text{Stern}}(x)$ ). The induced polarization due to the surface charge density at the monolayer–electrolyte interface ( $\bar{P}_E(x)$ ) is evaluated from the application of Gauss’ law to the electrostatic model of the monolayer–electrolyte interface in Figure 3c, yielding

$$\frac{\bar{P}_E(x)}{\epsilon_0} = \frac{\sigma_{\text{Stern}} - \epsilon_0 \bar{E}^{\text{diff}}(x)}{\epsilon_0} = \frac{\sigma_{\text{Stern}}}{\epsilon_0} \left( 1 - \frac{\epsilon_0}{\epsilon_d} \right) \quad (8)$$

where  $\epsilon_d$  is the dielectric permittivity of the diffuse part of the double layer and  $\sigma_{\text{Stern}}$  is the surface charge density at the

monolayer–electrolyte interface. Therefore, the microscopic electric field experienced by an electron in the monolayer film is given by

$$\bar{E}_{\text{micro}}^{\text{monolayer}}(x) = \frac{\bar{P}_E(x)}{\epsilon_0} = \frac{\sigma_{\text{Stern}}}{\epsilon_0} \left( 1 - \frac{\epsilon_0}{\epsilon_d} \right) \quad (9)$$

For anodic potentials, where  $\sigma_{\text{Stern}} < 0$ , the microscopic electric field in the monolayer, as calculated from eq 9, is comparable to the macroscopic field in magnitude ( $|\bar{E}| = \sigma_M/\epsilon_M$ ) but directed away from the monolayer–electrolyte interface. Similarly for cathodic potentials, the microscopic field is on the order of the observed electric field but directed opposite to the averaged macroscopic field and toward the monolayer electrolyte interface. Therefore, the net microscopic electric fields experienced by an electron at the gold–monolayer ( $\bar{E}_{\text{micro}}^{\text{monolayer}} + \bar{E}_{\text{micro}}^{\text{metal}}$ ) and monolayer–functional group interface ( $\bar{E}_{\text{micro}}^{\text{monolayer}} + \bar{E}_{\text{micro}}^{\text{Stern}}$ ) are both negligible. Consequently, there is no large abrupt change in the microscopic potential at these interfaces. Hence, we conclude that the metal–monolayer and monolayer–functional group contacts for all gold–monolayer–electrolyte systems are Ohmic in charge injection behavior because of barrier lowering by electrolyte polarization. There is, however, a barrier to charge transfer at the functional group–electrolyte interface, which constitutes the charge transfer barrier at the monolayer–electrolyte interface.

## Experimental Details

**Preparation of Monolayer Surfaces.** *n*-Alkyl thiols ( $\text{CH}_3(\text{CH}_2)_n\text{-SH}$ , where  $n = 9, 10, 11, 14, 15, 17$ ), 11-mercaptoundecanoic acid, 16-mercaptohexanoic acid, and 11-mercapto-1-undecanol were purchased from Sigma Aldrich for use in these experiments. These thiol molecules were dissolved in absolute ethanol (Pharmaco-Aaper, Shelbyville, KY) to form a dilute (1 mM) incubation solution. Long alkane chain thiol molecules, such as 1-octadecane thiol (Sigma Aldrich, St. Louis, MO), that were only partially soluble in ethanol were dissolved in a 2:3 mixture of toluene (analytical grade, Sigma Aldrich, St. Louis, MO) and absolute ethanol. SPR quality glass slides (GenTel Biosciences, Madison, WI), coated with evaporated chrome (5 nm) and gold (100 nm) thin films, were washed in a heated SC-1 bath (100 mL DI water/25 mL  $\text{H}_2\text{O}_2$ /2 mL  $\text{NH}_4\text{OH}$ ) and rinsed thoroughly with DI water and ethanol. The DI water (resistivity 18  $\text{M}\Omega\text{-cm}$ ) source was an in-house line. These gold surfaces were left to incubate in a parafilm-sealed beaker in the solution of thiol molecules for 48 h within a class 1000 cleanroom. The thiol-coated surfaces were rinsed thoroughly with ethanol and DI water and blow-dried with dry  $\text{N}_2$  before use. XPS on the monolayer-modified surfaces was performed with a Kratos Axis ULTRA X-ray photoelectron spectrometer using a Al X-ray source at 225 W, and the spectra were compared with published data<sup>38,39</sup> to verify the presence of the monolayer film. The XPS data also ruled out any evidence of possible defects (double bonds, foreign donor/acceptor species) in the alkane structure.

**Electrochemical Instrumentation and Measurements.** Electrochemical measurements were performed using a GAMRY Femtostat (Gamry Instruments, Warminster, PA) employing a three-electrode cell: the monolayer-coated gold surface acted as the working electrode, a Ag/AgCl wire in 3 M KCl (Bioanalytical Instruments, West Lafayette, IN) was the reference, and a gold or platinum wire was used as the counter. Platinum was used as the counter electrode for all surface area measurements and for a few of the impedance experiments. Gold

counter electrodes were used for most of the impedance measurements. The effect of the material and diameter of the counter electrode was found to be insignificant when impedance experiments with different counter electrodes were compared. All potentials are reported with respect to the Ag/AgCl reference. The working electrode was clamped in position using a vertical stage such that a constant area of the gold slide was immersed in the electrolyte solution. Electrolyte solutions for the impedance experiments were prepared as a ratio of mono- and dihydrogen potassium phosphate salts (Sigma Aldrich, St. Louis, MO) in DI water such that the total salt concentration and pH of the bulk electrolyte were as specified. All electrolyte solutions were degassed with nitrogen for an hour prior to the experiment. The potential spectrum of the low frequency impedance values was recorded by stepping the DC bias through increments of 25 mV between the limits of  $-500$  and  $500$  mV. The remaining points in the spectra plotted here are obtained by a cubic spline interpolation between the recorded data. We verified the accuracy of the spline interpolation by reducing the increment size to 5 mV in the neighborhood of the PZF obtained from the interpolated curve. The PZF realized from the smaller increments differ from the interpolation result by  $\pm 5$  mV. This error includes the variance due to composition of the electrolyte, electrode variability, and the error due to the interpolation curve.

## Results and Discussion

The admittance methodology we developed<sup>26</sup> is applied here to describe the current potential behavior of gold–monolayer–electrolyte systems for cases when the electrolyte does not contain any redox-active species. The potential regimes are described as “anodic” and “cathodic” with respect to the PZF (Figure 1). The low-frequency impedance response of the gold–monolayer–electrolyte system in the anodic potential regime is predominantly capacitive (Figure 2a). Thus, the observed current density in the system is limited by the rate of charge transport through the monolayer structure as discussed before. In addition, the conduction current exceeds the diffusion current for applied anodic potentials when  $V$  is greater than  $V_{\text{PZF}}$ , and the calculated conduction current is shown, in section i, to follow well-characterized solid-state charge transport models of Ohmic conduction at low electric fields and space-charge-limited conduction for higher fields. For extremely large electric fields in the monolayer ( $\sim 5 \times 10^8$  V/m) where  $V$  is much greater than  $V_{\text{PZF}}$ , the observed current density is shown in section ii to arise due to the quantum mechanical tunneling of the electron from the ground-state energy level of an ion in the electrolyte to empty electronic states in the metal phase, and the barrier height limiting the tunneling process characterizes specific properties of the monolayer–electrolyte interface. The cathodic potential regime, on the other hand, is characterized by a reduction current, in which electrons are transferred from the metal phase to the electrolyte solution. The low frequency impedance of the gold–monolayer–electrolyte system for cathodic potentials has a significant real component, thus indicating that the flow of charge through the system is limited by the charge transfer barrier at the monolayer–electrolyte interface (Figure 2b). The diffusion contribution is shown, in section iii, to dominate over the conduction current density at cathodic potentials in which  $V$  is much less than  $V_{\text{PZF}}$ , and for large negative overpotentials ( $> -150$  mV) displays the characteristics associated with the thermal excitation of electrons over an electrostatic potential energy barrier. The barrier height that limits hopping of electrons is determined by the chemistry of the functional end group and properties of the electrolyte

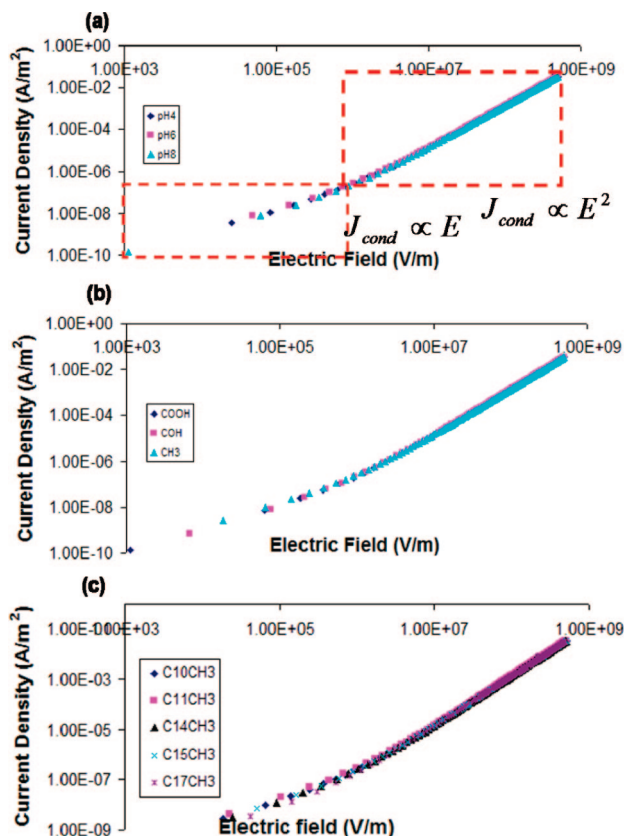


**Figure 4.** Conduction current density as a function of monolayer electric field for (a) variable electrolyte pH, (b) different monolayer functional groups, and (c) variable monolayer film thickness. For all experiments, the electrolyte is an aqueous 10 mM phosphate buffer solution maintained at pH 8 unless otherwise mentioned. The monolayer is self-assembled 1-mercaptodecanoic acid on gold in part a, and in part b, all monolayer films are 10 methylene units long. The regimes for Ohmic and space-charge-limited conduction are also delineated in part a.

solution. However, as shown in section iv, for small deviations of  $V$  less than  $V_{PZF}$ , the reorganization of the solvent around the reactants within the electrolyte limits the diffusion current density.

**i. Charge Conduction in the Monolayer (for  $V > V_{PZF}$ ).** The primary contribution to the oxidation current density for potentials that are anodic relative to the PZF comes from conductive transport, as mentioned before. Thus, the discussion in this section is focused mainly on the analysis of this conductive contribution. The average conduction current ( $J_{cond}$ ) in the monolayer is calculated from the expression

$$J_{cond} = \frac{\mu E}{\beta} \int_{-\beta}^0 \rho(x) dx \quad (10)$$

where  $\beta$  is the thickness of the monolayer. The conductive current density as a function of the electric field in the monolayer is depicted as a log-log plot in Figure 4a. The systems are 1.4 nm long, carboxylic acid-terminated alkane thiols in contact with electrolyte solutions maintained at three different values of bulk pH. The similarity in the curves for each of the three systems indicates that the mechanism of conductive transport in the monolayer is relatively independent of the bulk electrolyte properties such as pH and concentration and is primarily a function of the electric field in the monolayer. Moreover, the mechanism of charge conduction in the monolayer phase is also essentially independent of the functional end group (Figure 4b) and the length of the alkane chain (Figure 4c). As seen in Figure

4a, there are two regimes of conductive charge transport, depending on the strength of the electric field in the monolayer. At low electric fields ( $E < 1 \times 10^6$  V/m), the current density ( $J_{cond}$ ) is proportional to  $E$ , where the average monolayer conductivity ( $\sigma_{cond}$ ) is defined as

$$\sigma_{cond} = \frac{\mu}{\beta} \int_{-\beta}^0 \rho(x) dx \quad (11)$$

The conductivity was shown to be independent of the monolayer thickness<sup>26</sup> and was comparable to the reported low-field conductivity values of alkanethiol monolayers measured from solid-state metal-insulator-metal junctions ( $\sim 10^{-15}$  S/cm). The ohmic conduction in the monolayer film is facilitated by thermal free electrons within the monolayer film. These electrons are generated by the thermal excitation of electrons from the injecting contact (namely, the monolayer-electrolyte interface) into the LUMO of the alkane phase over the reaction-free barrier between the immobilized ions in the Stern layer and the functional group of the monolayer film. The number per unit volume ( $n_{Ohmic}$ ) of these electrons can be calculated from the Ohmic charge density  $\rho_{Ohmic}$  as

$$n_{Ohmic} = \frac{\rho_{Ohmic}}{e} = \frac{\sigma_{cond}}{e\mu} \sim 5 \times 10^{14} \quad (12)$$

For larger electric fields ( $1 \times 10^6 < E < 5 \times 10^8$  V/m), the conduction current is observed to be dependent on the square of the electric field ( $J_{cond} \sim E^2$ ). This parabolic functional dependence is characteristic of space-charge-limited current, in which the drift of the current carrying electronic charge is punctuated by frequent collisions with the thermal vibrations of the methylene moieties in the alkane backbone and with other electrons that are injected by diffusion into the monolayer phase due to the difference in electron density at the metal-monolayer and monolayer-electrolyte interfaces.<sup>40,41</sup> The diffusion-injected charge due to the electron concentration difference at the two interfaces and the thermal vibrations constitute the space charge that limit the conductive transport of electrons in the monolayer. The space-charge-limited current (SLC) density can be evaluated from

$$J_{SLC} \propto \frac{\epsilon_M \mu}{L} E^2 \quad (13)$$

where the constant of proportionality is on the order of 1.<sup>42</sup> In eq 13,  $L$  represents the penetration length for the space charge, that is, the extent to which the diffusion-injected charge and thermal vibrations influence the current flow, measured as a distance from the injecting contact.<sup>42</sup> A larger value of  $L$  signifies a greater number density of diffusion-injected charge in the monolayer or a larger hindrance to the transport of electrons due to collisions with the thermal vibrations of the alkane chains. Thus, the penetration length is an intrinsic measure of the ability of the monolayer phase to carry space charge and, hence, limit the flow of current. This phenomenological length scale arises in thin-film systems in which the charge density is observed to fall exponentially (Figure 5a) to the thermal free charge density ( $\rho_{Ohmic}$ ).<sup>42</sup> The functional form of the charge density, calculated by solving the first-order differential equation for the real admittance component in eq 1, follows the profile shown in Figure 5a.

The penetration length should be some fraction of the length of the alkane chain in the monolayer phase and cannot be larger than the thickness of the monolayer film, i.e.

$$L = \kappa\beta \quad (\kappa \leq 1) \quad (14)$$

For large electric fields near the maximum of the space-charge-limited current regime, when the injection due to the

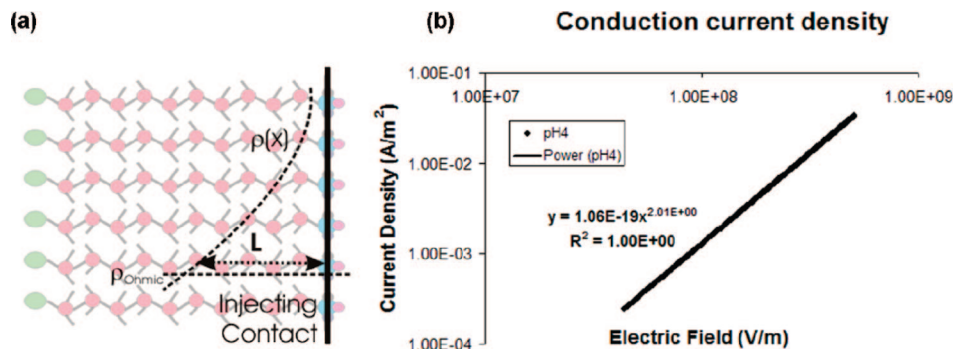


**Figure 5.** (a) Schematic illustrating the physical significance of penetration length,  $L$ . For the oxidation reactions at these anodic potentials, the monolayer–electrolyte interface serves as the electron injection contact. (b) A two-parameter power law best fit for the conduction current density is shown here. The monolayer film is 1-mercaptodecanoic acid self-assembled on gold, and the electrolyte is a 10 mM aqueous phosphate buffer solution maintained at pH 4.

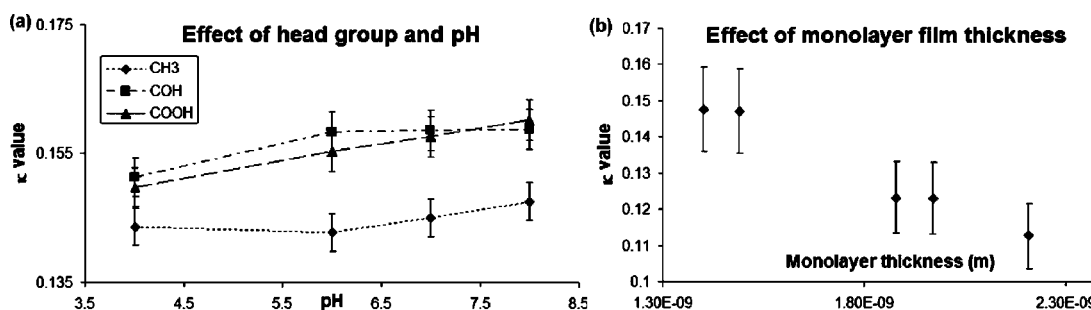


**Figure 6.**  $\kappa$  values for space charge current as functions of (a) electrolyte pH and functional end group and (b) monolayer film thickness. For the experiments in part a, the monolayer film is 10 methylene units thick and the electrolyte is a 10 mM phosphate buffer solution. In part b, the alkane chains are all terminated by methyl functional groups and the electrolyte solution is a 10 mM phosphate buffer solution maintained at pH 8. Markers in part a are connected by dotted lines to clarify the graph.

applied field overwhelms the intrinsic ability of the monolayer film to hold space charge, the penetration length for all gold–monolayer–electrolyte systems would simply be equal to the thickness of the monolayer film. Since the upper bound on  $L$  is the monolayer thickness,  $\beta$  provides a convenient length scale parameter when using scaling arguments to calculate  $\mu$  and  $D$ , as discussed in reference 26. The intrinsic space charge in the monolayer film is a function of the length of the alkane backbone because an electron drifting through a thicker monolayer film experiences many more collisions with thermal vibrations of the alkane chains. The difference in chemical potential between an electron at the metal and at the IHP also affects the space charge, since a larger chemical potential difference increases the amount of electronic charge that is injected into the monolayer film by a thermal diffusion process. Thus, the factor  $\kappa$  in eq 14 has a physical significance and represents the contribution to the space charge from the thermal diffusion of electrons into the monolayer film.

Substituting eq 14 into eq 13 and assuming the proportionality constant to be unity, we get

$$J_{\text{SCL}} = \frac{\varepsilon\mu}{\kappa\beta} E^2 \quad (15)$$

The value of  $\kappa$  in eq 15 is obtained by fitting the conductive current density plot in the space–charge–limited regime with a function of the form  $\gamma x^\zeta$ , where  $\gamma$  and  $\zeta$  are constants determined by the least-squares fit (Figure 5b). For all gold–monolayer–electrolyte systems considered here,  $\zeta \sim 2$ ; the values of  $\kappa$ , calculated from the values of  $\gamma$ , are shown in Figure 6. As expected, the trends observed indicate that more electronegative head groups result in larger  $\kappa$  values due to greater differences in chemical potential (Figure 6a). Increased electrolyte pH

should have a similar effect on  $\kappa$ . However, the observed increase in  $\kappa$  with electrolyte pH is not statistically significant enough to make that conclusion. The thickness of the monolayer film results in decreasing chemical potential differences, and thus,  $\kappa$  decreases with increasing alkane chain length (Figure 6b). The steps in the values of  $\kappa$  superimposed on the overall decreasing value are due to the even–odd effect of the alkane phase.<sup>26</sup>

**ii. Electron Tunneling Events at the Monolayer–Electrolyte Interface ( $V \gg V_{\text{PZF}}$ ).** The low frequency impedance response of a gold–monolayer–electrolyte system begins to acquire a small real component for large anodic potentials as compared to the electrical response observed for potentials that are only a few hundred millivolts greater than the PZF.<sup>26</sup> The small but statistically significant shift in response indicates an increasing contribution from the charge transfer barrier at the monolayer–electrolyte interface to the rate-limiting step in the charge flow process, as discussed before. The observed current density–electric field curves begin to display quantum mechanical tunneling effects when the electric field in the monolayer is larger than  $5 \times 10^8$  V/m. The linear relation between the variables  $E \cdot \ln(J/E^2)$  vs  $E$  in Figure 7a is characteristic of Fowler–Nordheim tunneling, in which the potential barrier to electron transfer at the IHP is distorted by the large electric fields such that the electron wave function can penetrate through the reduced barrier, across the empty conduction band of the monolayer phase, and into the empty recipient states in the bulk metal (Figure 7b). This rate-limiting electron transfer event at the monolayer–electrolyte interface gives the impedance response a small real component. The Fowler–Nordheim current density ( $J_{\text{FN}}$ ) expression is a probabilistic description of an electron wave tunneling through a triangular potential barrier

from occupied states at the IHP on one side of the barrier to empty states in the bulk metal at the other end,<sup>43–48</sup> i.e.

$$J_{\text{FN}} = \int F_f \frac{N_f}{2(2m^*(\epsilon_i))^{1/2}} F_e P(\epsilon') d\epsilon' d\epsilon_i \quad (16)$$

where  $N_f$  and  $F_f$  are the density and the occupation probabilities of the occupied states in the above expression;  $F_e$  is the probability that the recipient state in the bulk metal is empty;  $m^*$  is the effective electron mass;  $\epsilon_i$  and  $\epsilon'$  are the total energy of the electron and the energy of the electron perpendicular to the interface, where both energies are with reference to the LUMO level;  $P(\epsilon')$  is the probability that electrons with perpendicular energy  $\epsilon'$  can penetrate the potential barrier; and the factor in the denominator of the integrand represents the normal scattering velocity with which electrons strike the monolayer–electrolyte interface.<sup>49</sup> The states at the IHP that supply the electron to the monolayer conduction band at these large anodic potentials would correspond to partially hydrated anions localized at the Stern layer, and these immobilized anions exchange with the ions in the bulk electrolyte primarily by a thermal activation process. We will, henceforth, refer to these immobilized ions together with their partial solvent shell as “electrolyte states.” The field emission of electrons from a metal surface into vacuum considered in the seminal work by Fowler et al.<sup>44</sup> is significantly different from the electron tunneling from the electrolyte states into the empty metal states. However, the two processes are shown to be qualitatively and quantitatively very similar under a certain set of assumptions discussed below.

All electron transfer events between species in solution consist of nuclear vibration-induced fluctuations in the electron energy levels of the donor and the acceptor moieties, followed by the tunneling of the transferring electron once the energy levels of the two species align.<sup>50</sup> The nuclear motion discussed here includes vibrations internal to the molecular species caused by thermal excitation of the individual atoms constituting the species and external vibrations due to interactions with the surrounding medium. Therefore, the probability that an electron tunnels is closely linked to the thermal vibrational motion of nuclei of reacting species and the medium that creates the necessary preconditions for the tunneling of an electron; that is, the quantities  $N_f$  and  $F_f$  in eq 16 are functions of the nuclear coordinates and momenta that can be determined only by the simultaneous solution of the electronic and nuclei Hamiltonians. For slow-moving nuclei, electron energy level degeneracy between the donor and acceptor species remains for a sufficiently long time such that tunneling between the moieties is probabilistically certain. Thus, the rate expression describing the

process (and the current density) is dependent only on the energetics of the slow moving reactant nuclei and solvent media.<sup>51</sup> Conversely, an electron transfer system characterized by fast-moving nuclei and high potential energy barriers between the degenerate energy levels is rate-limited by the electron tunneling between the reacting species. Donor anionic electrolyte states at the Stern layer are, as expected, characterized by rapid thermal vibrations of the constituent nuclei because these species usually exist in solution as dehydrated (or weakly hydrated) ions,<sup>52</sup> and as they adsorb at the Stern layer, these anions tend to lose their hydration spheres. The substantially reduced solvent shell around the anions at the Stern layer facilitates the high speed motion of individual atoms making up the anion. Consequently, the rate expression for the observed oxidation current density appears as a probabilistic description of a tunneling event from the energy level of an immobilized anion to the empty states of the metal phase, where the electric field acts to distort the energy levels of the accepting functional groups in the monolayer film such that there is significant overlap between LUMO of the monolayer film and the excited energy levels of the anionic species. As the electric field increases in magnitude (for increasingly anodic applied potentials), this distortion becomes large enough to induce an overlap between the LUMO and the ground-state energy levels of the immobilized ions, thereby facilitating electron tunneling without necessitating the alignment of energy levels by thermal excitation. Thus, sufficiently large electric fields enable tunneling even from anionic species such as hydroxyl ( $\text{OH}^-$ ) ions that exist as partially solvated ions at the Stern layer.<sup>52</sup>

In addition, the electrons in the electrolyte states are assumed to follow classical distribution statistics,<sup>6,53,54</sup> and thus, the corresponding density of states for electrons occupying molecular orbitals in the electrolyte states is given by the form<sup>55</sup>

$$N_f \propto (\epsilon_i)^{1/2} \exp\left(-\frac{\epsilon_i}{kT}\right) \quad (17)$$

Another simplifying assumption that must be highlighted in eq 16 is that the expression for quantum mechanical tunneling current density does not contain any factor to account for the interaction of the tunneling electron with electrons in the LUMO of the monolayer phase. Assuming that the electrons follow classical statistics, there is almost no possibility that the electrons can be thermally injected into the LUMO from the HOMO of the alkane chains because the energy gap between the two sets of orbitals ( $\sim 8$  eV)<sup>56</sup> is much larger than the thermal energy of the electrons ( $\sim 0.025$  eV). Thus, the probability that states in the conduction band of the monolayer phase would be empty

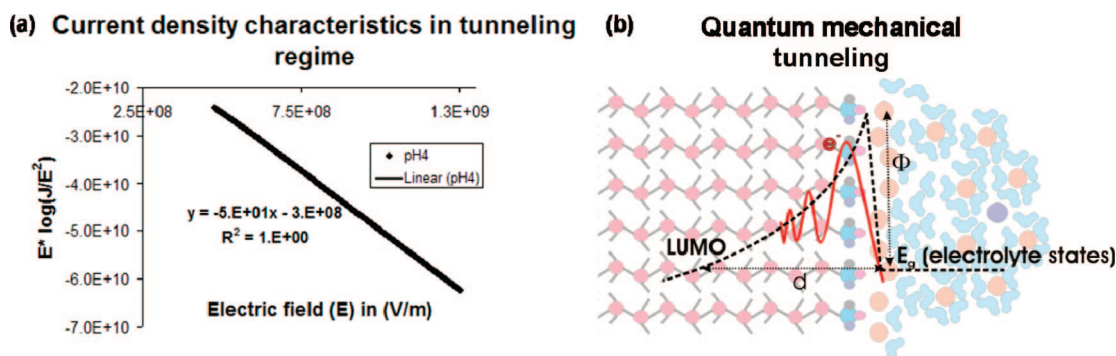


**Figure 7.** (a) Linear dependence of the Fowler–Nordheim parameter,  $E \cdot \ln(J/E^2)$ , on the monolayer electric field ( $E$ ), for large ( $> 5 \times 10^8$  V/m) electric fields, is illustrated in this graph. The system is a monolayer of 1-mercaptodecanoic acid on gold, in contact with a 10 mM phosphate electrolyte solution, buffered at pH 4. (b) Schematic depicting the quantum mechanical tunneling process from the ground energy level of the electrolyte states ( $E_g$ ) into the monolayer conduction band (LUMO).

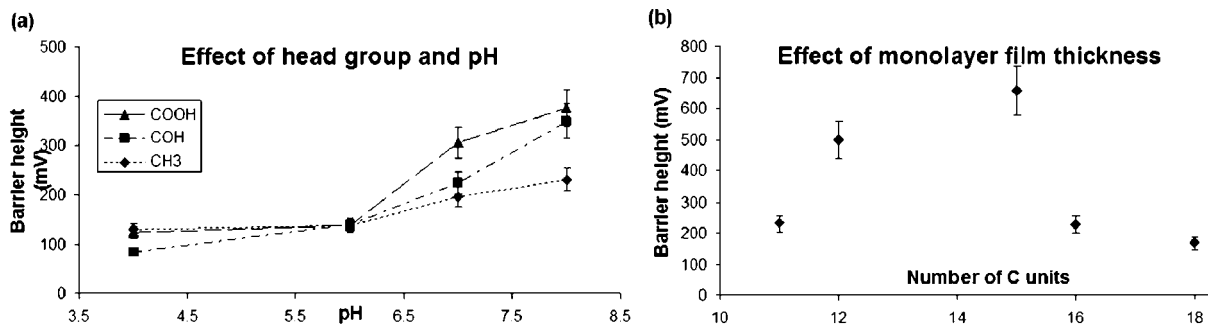


**Figure 8.** Fowler–Nordheim tunneling barriers as functions of (a) electrolyte pH and functional end group and (b) the number of methylene units in the alkane backbone. For the experiments in part a, the monolayer film is 10 methylene units thick and the electrolyte is a 10 mM phosphate buffer solution. In part b, the alkane chains are all terminated by methyl functional groups and the electrolyte solution is a 10 mM phosphate buffer solution maintained at pH 8. Markers in part a are connected by dotted lines to clarify the graph.

for the lifetime of the tunneling process is nearly one. The tunneling current density calculated in eq 16 under these assumptions (see Supporting Information) has a form very similar to the expression derived by Fowler and Nordheim in their paper describing field emission of electrons from metals,<sup>44,45</sup> such that

$$J_{\text{FN}} \propto E^2 \exp\left(-\frac{4(2m^*)^{1/2}\Phi^{3/2}}{3\hbar eE}\right) \quad (18)$$

where  $e$  is the electron charge,  $\hbar$  is the modified Planck constant, and  $\Phi$  is the intrinsic potential energy barrier to the tunneling process (Figure 7b). Here, the effective electron mass,  $m^*$ , is considered equal to the free electron mass  $m_e$ . The barrier height can now be evaluated from the intercept in the plot of  $E \cdot \ln(J/E^2)$  versus  $E$ .

The intrinsic potential energy barrier in eq 18 is a measure of the characteristic electric field that determines the onset of the tunneling process. This electric field is given by the numerator of the exponential factor in eq 18 as

$$E_{\text{tunn}} = \frac{4(2m^*)^{1/2}\Phi^{3/2}}{3\hbar e} \quad (19)$$

where  $E_{\text{tunn}}$  characterizes the extent of distortion required in the rectangular barrier before tunneling can occur. This distortion is a function of the electrostatic and steric interactions between the electron exchanging surface sites at the monolayer functional groups and the electrolyte states. The interaction between these species has a strong influence on the distance of closest approach between the anions and the surface sites and, therefore, limits the electron transfer process. The distortion is also dependent on the width the electron has to traverse within the barrier region ( $d$  in Figure 6b). An infinitely high electrostatic or steric interaction energy barrier or a very wide barrier region would reduce the tunneling current to zero.<sup>43</sup> Since tunneling is a probability-based description of the transfer of an electron from filled to empty states across the intrinsic potential energy barrier, the variables affecting the height of the intrinsic potential barrier can be separated out as shown,

$$\Phi \propto f(d) g(\phi) \quad (20)$$

where  $f(d)$  represents the factors affecting the width of the barrier region, and  $g(\phi)$  is a function of the variables affecting the electrostatic and steric interactions between surface sites at the monolayer and the electrolyte states. Therefore, the function  $g(\phi)$  depends on the chemistry of the surface sites and the electrolyte states. Increasing the electronegativity of the functional groups enhances the repulsive Coulombic environment between the anionic electrolyte states and the functional groups

at the monolayer–electrolyte interface, thereby increasing the barrier height (Figure 8a).

As discussed before, the electronic energy levels in the immobilized electrolyte states of the Stern layer that participate in the charge transfer/tunneling process at the monolayer–electrolyte interface correspond to the vibration energies of the constituent atoms or of the ion–solvent bonds<sup>53</sup> in the case of the hydroxyl radical. An elegant argument put forward by Gurney<sup>54</sup> showed that the highest occupied vibrational energy level for an anion is lower than the lowest unoccupied state for a hydrated cation. Thus, increasing the concentration of the electron carrying species in the electrolyte ( $\text{OH}^-$ ,  $\text{H}_2\text{PO}_4^-$ ,  $\text{HPO}_4^{2-}$ ) by increasing the bulk electrolyte concentration or pH decreases the ground-state energy level of the electrolyte from which tunneling occurs, thereby increasing the effective barrier to the tunneling process (Figure 8a). The barrier is largest for the methyl-terminated moiety and smallest for the electronegative alcohol group at low electrolyte pH (Figure 8a), possibly indicating that a steric hydrophobic interaction potential exists between the surface sites on the functional group and the immobilized ions at the outer Helmholtz plane. The distance of closest approach for the ions in the electrolyte to the inner Helmholtz plane is, seemingly then, determined by the polar water molecules that are hydrophobically repelled by the methyl group and are favorably attracted to the alcohol group via a hydrogen bonding mechanism. However, similar to the methyl functional group, a large barrier is also observed for the protonated carboxylic acid moiety at low pH, even though the protonated carboxylic acid functional group can form hydrogen bonds with the electrolyte solvent. Our hypothesis for this supposed discrepancy is that the hydroxyl ( $-\text{OH}$ ) subunit on the carboxylic acid group appears to act as the electron-accepting surface site, and the planar structure of the  $\text{sp}^2$  hybridized carboxylic acid moiety causes significant overlap between the  $=\text{O}$  and the  $-\text{OH}$  subunits on neighboring carboxylic acid functional groups. The spatial overlap between the two subunits from neighboring functional groups restricts access for the electron donating anion to the  $-\text{OH}$  species on the carboxylic moiety. The increased Coulombic repulsion for the electronegative head groups at higher pH values dominates over the steric/hydrophobic forces, and the two forces appear to balance each other around pH 6 (Figure 8a). The switch in the barrier associated with the carboxylic acid functional group, from a methyl moiety like barrier at low pH to an alcohol functional group-like barrier at higher pH, can be ascribed to the deprotonation of the acid group at higher pH values,<sup>57,58</sup> which makes the negatively charged carboxylic acid group comparable to the alcohol moiety in electronegativity. The deprotonated carboxylic

acid has an  $sp^2$  hybridized resonance stabilized structure, in which the negative charge is delocalized on the two oxygen species. Thus, the two deprotonated oxygen moieties are equivalent as surface sites from the perspective of the electron donating anionic species at the Stern layer. The primary contribution to the barrier height, in the case of the carboxylic acid functional group, comes from the Coulombic repulsion due to the negative charge and not from a steric effect. Our hypothesis for the unique behavior of the carboxylic acid functional group appears to explain, albeit qualitatively, the dependence of the tunneling barrier height with pH for the  $sp^2$  hybridized moiety. However, the experimental evidence in terms of the pH dependent tunneling barrier height is not sufficient enough to conclusively establish that the  $-OH$  species on the carboxylic functional group is, indeed, the electron accepting site or that overlap between  $=O$  and the  $-OH$  subunits on neighboring carboxylic acid functional groups hinders the electron transfer event. We refer again to this description of the overlapping  $sp^2$  hybridized structure of the carboxylic acid moiety in sections iii and iv of this paper to demonstrate the effect of the structure of the carboxylic acid functional group on two different experimental parameters; namely, the coupling coefficient ( $\alpha$ ) and the reorganization energy ( $\lambda$ ) for the electron transfer reaction. Our hypothesis for the structure of the carboxylic acid functional group requires further verification by an orthogonal experimental technique that can probe the structure of a monolayer–electrolyte interface. Nonetheless, by appealing to this description, we are able to qualitatively explain three different and unrelated experimental observations; namely, the tunneling barrier height ( $\Phi$ ), the coupling coefficient ( $\alpha$ ), and the reorganization energy ( $\lambda$ ). The thickness of the monolayer film is a factor that affects the width of the barrier region ( $d$ ), and thus, the tunneling barrier should increase with the number of carbon atoms in the alkane backbone of the monolayer phase. However, above a certain threshold monolayer thickness, the barrier is seen to decrease rather rapidly with the number of carbon atoms (Figure 8b). As discussed in reference 26, the decrease in barrier height can be attributed to a decrease in Coulombic repulsion between the electrons at the surface sites and the electron gas in the metal and this reduces  $g(\varphi)$ . Thus, the net barrier height in Figure 8b is an interplay between the two functions in eq 20, where  $f(d)$  increases with the thickness of the monolayer film and  $g(\varphi)$  is a decreasing function of the number of carbon atoms in the monolayer phase.

The intrinsic potential energy barrier,  $\Phi$ , in eq 19 is obtained from the observed functional dependence of the net current density on the electric field in the monolayer, where both dependent ( $J$ ) and independent ( $E$ ) variables are measured quantities. Therefore, the intrinsic potential barrier is also an experimentally measured quantity that is dependent on electrolyte properties (Figure 8a), even when the monolayer functional group and length of the alkane backbone are not varied. This observation suggests that the barrier to electron transfer exists at the monolayer–electrolyte interface and that any barrier to charge transfer at the gold–monolayer interface is comparatively insignificant.<sup>59,60</sup> In addition, if the barrier to charge transfer did exist at the metal–monolayer interface, as would be the case for large pinhole defects in the monolayer film, tunneling of electrons would occur from the vibrational energy levels of the ions in the pinhole structures to the metal Fermi level and, therefore, would be dependent on the electric field in the metal phase and *not* on the electric field in the monolayer structure, as observed in Figure 7a.

The current–electric field dependence transitions from functional forms that characterize charge transport in thin films at low and intermediate electric fields to a form with a wavelike propagation of charge across an energy barrier at the Stern layer at high electric fields. This change in character suggests that charge transport through the monolayer phase is the rate-limiting step at low and intermediate electric fields and that for larger electric fields, the process of quantum mechanical electron transfer across the monolayer–electrolyte interface becomes the rate-determining mechanism. This observation is also borne out by an inspection of the impedance plots discussed above. For the potential regime characterized by a capacitive response, the net current density is limited by the rate of transport of charge through the monolayer phase. For the potential regime in which the impedance has a small real component, the net current density is limited partly by charge transfer occurring at the monolayer–electrolyte interface. Electric field-induced quantum mechanical tunneling of electrons from the ground state of the anions to the empty metal states cannot be classified only as a charge-transfer-barrier-limited event because this process involves the propagation of a wavelike electron through an energy barrier that extends across the width of the monolayer phase. Therefore, the phenomenon of electron tunneling resembles both a charge transport and a charge transfer process between the functional end group and the anion at the Stern layer. The distinction between a charge transfer event and the tunneling of electrons across a potential energy barrier at the monolayer–electrolyte interface is reflected in the dependence of the tunneling barrier on transport parameters such as the monolayer thickness and also in the phase of the impedance response that shows a small deviation from  $-90^\circ$  at low frequencies.

For potential regimes in which the current is limited by the number of thermal carriers or by space charge, the kinetics of the electron transfer process at the Stern layer is relatively fast. Therefore, the surface sites at the monolayer functional groups are in equilibrium with the anionic electrolyte states at the Stern layer. The anionic electrolyte states are, in turn, assumed to be at equilibrium with the bulk electrolyte solution (see Supporting Information), where the distribution of anions in the diffuse part of the double layer is given by the classic Poisson–Boltzmann form. Consequently, the surface sites at the monolayer functional group are also at equilibrium with the bulk electrolyte solution. Thus, parameters such as the built-in and equilibrium electric fields, which characterize the monolayer–electrolyte interface, display a linear increase with bulk electrolyte pH and the log of bulk electrolyte concentration.<sup>26</sup>

**iii. Diffusion-Limited Currents (for  $V \ll V_{PZF}$ ).** The average diffusion current is the main contributor to the net reduction current density for potentials that are sufficiently more cathodic than the PZF. The average diffusive component can be evaluated from

$$J_{\text{diff}} = J_{\text{total}} - \frac{\mu E}{\beta} \int_{-\beta}^0 \rho \, dx \quad (21)$$

The diffusion current is plotted as a semilog function of the applied potential for this limited range of potentials in Figure 9a, for a 1.4-nm-long carboxylic acid-terminated monolayer system in contact with three different electrolyte solutions maintained at different bulk pH values. The diffusion current varies exponentially with applied potential to a reasonable degree of correlation (regression coefficient  $\sim 0.98$ ), and this functional dependence is independent of the nature of the functional end group (Figure 9b) and the length of the alkane chain (Figure 9c). The similarity in the functional dependence on potential

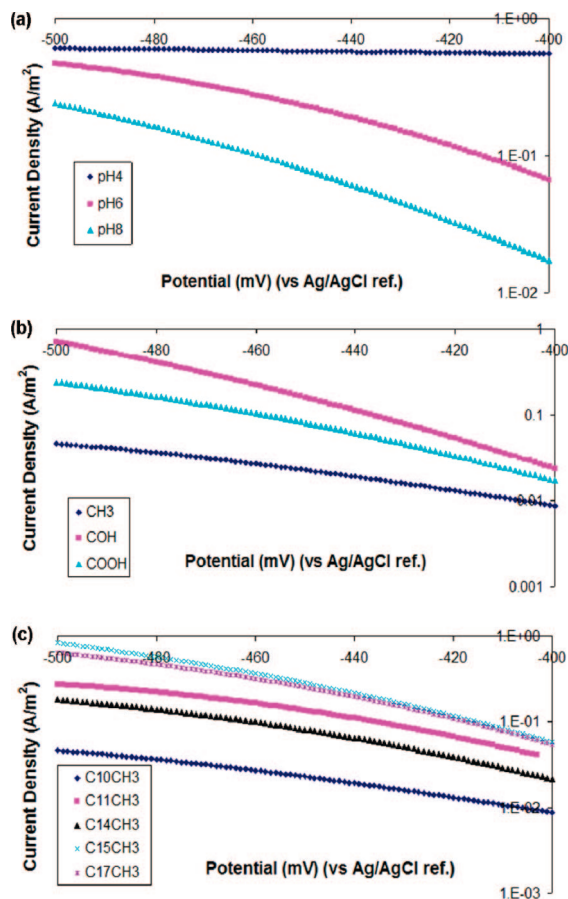


**Figure 9.** Diffusion current density as a function of monolayer electric field for (a) variable electrolyte pH, (b) different monolayer functional groups, and (c) variable monolayer film thickness. For all experiments, the electrolyte is an aqueous 10 mM phosphate buffer solution maintained at pH 8 unless otherwise noted. In addition, in part a, the monolayer is self-assembled 1-mercaptodecanoic acid on gold, and in part b, all monolayer films are 10 methylene units long.

suggests a common mechanism for the diffusive transport of charge that is independent of the bulk electrolyte properties, alkane chain length, and functional end group, as in the previous section. The exponential nature of the functional dependence of diffusion current on applied potential suggests a thermionic emission-like mechanism of electron transport for these potential regimes; that is, the net current is limited by the rate at which transported electrons are thermally emitted over the potential energy barrier between the surface sites and the electrolyte states at the monolayer–electrolyte interface,<sup>43,61–63</sup> and not by the transport of charge through the monolayer phase. The thermionic emission of charge is qualitatively similar to charge diffusion in that both processes involve the thermal activation of charge carriers across an energy barrier.<sup>43</sup> Thus, the diffusion current density in the gold–monolayer–electrolyte system at large cathodic potentials is a measure of the net kinetic energy of the transported electrons that overcome the potential barrier,<sup>43,62,63</sup> such that

$$J_{\text{diff}} = \int_{e\varphi_{\text{IHP}}}^{\infty} ev_x dn \quad (22)$$

where  $v_x$  is the velocity of the transported electrons along the direction of transport,  $n(\varepsilon_i)$  is the number density of these electrons as a function of the electron energy ( $\varepsilon_i$ ), and  $e\varphi_{\text{IHP}}$  is a measure of the minimum amount of energy required to overcome the energy barrier at the monolayer–electrolyte

interface.<sup>26</sup> An accurate estimate of the barrier height at the monolayer–electrolyte interface must take into account the contribution from the electrostatic potential at the outer Helmholtz plane ( $\varphi_{\text{OHP}}$ ), since the accumulated charge in the diffuse layer gives rise to an electric field that creates an electrostatic potential energy barrier between the bulk electrolyte and the outer Helmholtz plane. Simple scaling arguments demonstrate that this potential can be neglected in comparison to  $\varphi_{\text{M}}$  or  $\varphi_{\text{IHP}}$  (see Supporting Information). Using the assumption that the electrons in the monolayer conduction band follow classical statistics (see Supporting Information), the integral in eq 22 can be reduced to<sup>43</sup>

$$J_{\text{diff}} = c(T) \exp\left(-\frac{m^* V_0^2}{2kT}\right) \quad (23)$$

where  $V_0$  is the minimum velocity required to overcome the energy barrier at the Stern layer, and  $c$  is a temperature dependent constant derived from the exact density of states expression.<sup>43,55</sup> If we assume that the electron is transmitted elastically<sup>61</sup> through the monolayer phase from the metal to the IHP, then at large cathodic potentials, the minimum velocity  $V_0$  can be related to the applied potential ( $\varphi_{\text{M}}$ ) by an energy balance on the electrons such that

$$\frac{m^* V_0^2}{2} = -e(\varphi_{\text{M}} + \varphi_{\text{IHP}}) + \varepsilon_0' \quad (24)$$

where  $\varepsilon_0'$  is the baseline energy of the transported electron at the normal hydrogen electrode with respect to the vacuum reference level. Substituting eq 24 into eq 23 yields

$$J_{\text{diff}} = c(T) \exp\left(-\frac{\varepsilon_0'}{kT}\right) \exp\left(\frac{e(\varphi_{\text{M}} + \varphi_{\text{IHP}})}{kT}\right) \quad (25)$$

The finite charge size assumption,<sup>26</sup> with the resulting linear potential drop within the monolayer phase, can be used to relate  $\varphi_{\text{IHP}}$  to  $\varphi_{\text{M}}$ . However, this yields no additional physical insight into the large difference in slopes for the curves observed in Figure 9 other than there are differences in the monolayer electric field for different bulk electrolyte conditions, end groups, and alkane lengths. A methodology is developed below specifically to address this concern, where the potential dependence of the current is utilized to extract information about the charge transfer between the monolayer surface sites and the energy states of the electrolyte at the Stern layer.

Since the current is limited by the rate at which the electrons thermally hop over a potential energy barrier at the monolayer–electrolyte interface, the low-frequency impedance characteristics of gold–monolayer–electrolyte systems display significant real characteristics at large cathodic potentials, thereby indicating that an interface charge transfer process is rate-limiting (Figure 2b), as discussed before. For this potential regime, the electrolyte and monolayer phase are spatially decoupled from one another, because an electronic equilibrium would not exist between the electron donating surface sites on the monolayer functional groups and the electron accepting cationic electrolyte states. The cationic electrolyte states in the electrolyte are of two types: (a) reactive states that accept electrons from surface sites in the monolayer phase, and (b) accumulated cationic species that do not actively participate in the charge transfer process, though they contribute to the development of the charge transfer barrier ( $\sim e\varphi_{\text{IHP}}$ ) at the monolayer–electrolyte interface. The applied potential is divided between the monolayer phase and the Stern layer such that the ratio of the potential drops in the two regions is indicative of the ratio between the surface density of charged

species in the Stern layer that are created by charge transfer from the surface sites and the surface density of charged states that accumulate electrostatically within the Stern layer due to the electric field. Thus, for the limited range of large cathodic potentials, the field in the monolayer phase can now be approximated as a linear function of the applied potential where the slope ( $\alpha$ ) is shown to be a function of the number of reactive electrolyte states, accumulated electrolyte states, and the thickness of the monolayer film, such that

$$E\beta = \alpha\varphi_M \quad (26)$$

The expression for  $\alpha$  has the functional form  $\alpha = f(C_{sm}, C_{se}, \beta)$ , where  $C_{sm}$  and  $C_{se}$  are the respective capacitances of the reacted electrolyte states and accumulated electrolytic states and  $\beta$  is the thickness of the monolayer phase, as before. Since the negatively charged surface sites are reactive intermediates with lifetimes comparable to the relaxation time for electronic charge polarization ( $\sim 10^{-15}$  s)<sup>51</sup> and eq 26 is applied to low-frequency data ( $\sim 0.01$  Hz) only, the capacitance due to the surface sites does not feature independently in the functional form for  $\alpha$ , and is instead represented in the  $C_{sm}$  term. The potential at the IHP can now be described in terms of the constant  $\alpha$ ,

$$\varphi_{IHP} = \varphi_M - E\beta = (1 - \alpha)\varphi_M \quad (27)$$

Inserting eq 27 into eq 25 yields

$$J_{diff} = c(T) \exp\left(-\frac{\varepsilon_0'}{kT}\right) \exp\left(\frac{(2 - \alpha)e\varphi_M}{kT}\right) \quad (28)$$

where  $\alpha$  can be calculated from the slopes of the semilog curves in Figure 9. For the diffusion current to increase monotonically with increasingly cathodic potentials, as seen in Figure 9,  $\alpha$  should be larger than 2.

The functional form for  $\alpha$  is derived from the application of Gauss' law and charge conservation to the gold–monolayer–electrolyte system.<sup>64</sup> The total potential drop in the system is the sum of the potential drop in the monolayer phase ( $\Delta\varphi_i$ ), and the potential drop at the monolayer–electrolyte interface ( $\Delta\varphi_{Stern}$ ), which satisfies

$$\frac{d\Delta\varphi_i}{d\varphi_M} + \frac{d\Delta\varphi_{Stern}}{d\varphi_M} = 1 \quad (29)$$

At large cathodic potentials, the potential drop in the diffuse layer ( $\sim \varphi_{OHP}$ ) is ignored, as discussed before. Therefore, the only contribution to  $\Delta\varphi_{Stern}$  comes from  $\varphi_{IHP}$ , and eq 27 is used to evaluate the derivative  $d\varphi_{Stern}/d\varphi_M$  in eq 29 so that

$$\frac{d\Delta\varphi_{Stern}}{d\varphi_M} = 1 - \alpha \quad (30a)$$

which yields

$$\frac{d\Delta\varphi_i}{d\varphi_M} = \alpha \quad (30b)$$

The finite charge size approximation and the charge conservation equation are used together in the application of Gauss' law to evaluate the derivative on the LHS of eq 30b, giving

$$\frac{d\Delta\varphi_i}{d\varphi_M} \sim \frac{\beta}{\varepsilon_M} \left( \left[ \frac{d\sigma_{Stern}}{d\Delta\varphi_i} \frac{d\Delta\varphi_i}{d\varphi_M} + \frac{d\sigma_{Stern}}{d\Delta\varphi_{Stern}} \frac{d\Delta\varphi_{Stern}}{d\varphi_M} \right] + \left[ \frac{d\Delta\varphi_i}{d\varphi_M} \frac{d}{d\Delta\varphi_i} \int_{-\beta}^0 \rho \, dx \right] \right) = \alpha \quad (31)$$

The term in the first set of square brackets on the LHS of eq 31 is the total capacitance of the Stern layer. The Stern layer

capacitance is composed of the average capacitance of the reactive electrolyte states ( $C_{sm}$ ) that interact with the metal phase via the charge transfer process, in parallel with averaged capacitance due to the accumulated electrolyte states ( $C_{se}$ ) that interact only with the electrolyte phase, such that if the applied potential were to drop entirely across the Stern layer, it would drop in the ratio  $\alpha/(1 - \alpha)$  across the respective capacitors. The individual capacitance components ( $C_{sm}$  and  $C_{se}$ ) are averaged out with respect to the applied potential. Thus, rewriting the Stern layer capacitance term in eq 31, we get

$$\frac{d\sigma_{Stern}}{d\varphi_M} = C_{Stern} = \alpha C_{sm} + (1 - \alpha)C_{se} \quad (32)$$

The term in the second set of square brackets in eq 31 is a measure of the average capacitance of the monolayer ( $\sim \varepsilon_M/\beta$ ). Substituting eq 32 into eq 31 and simplifying yields

$$\alpha = \frac{C_{se}}{2\frac{\varepsilon_M}{\beta} + (C_{se} - C_{sm})} \quad (33)$$

A hypothetical gold–monolayer–electrolyte system in which the number of accumulated electrolyte states at the Stern layer tends to zero (i.e.,  $C_{se} \sim 0$ ) or, analogously, a system in which the monolayer phase is infinitesimally thin should result in a zero electric field in the monolayer because the IHP potential would follow the applied potential at the metal without the accompanying voltage drop in the monolayer phase. Equations 26 and 33 capture this asymptotic case. The condition  $\alpha > 2$  yields a lower bound on the values of  $C_{sm}$  and  $C_{se}$  such that

$$C_{sm} - \frac{C_{se}}{2} > \frac{2\varepsilon}{\beta} \quad (34)$$

Equation 34 indicates that the number of electrolyte states created by the reaction at the monolayer–electrolyte interface exceeds the number of capacitively accumulated electrolyte states in the Stern layer. Since the current at these cathodic potentials is a reduction current, the reactive electrolyte species are most likely partially hydrated protons that accept electrons from the surface sites on the monolayer functional groups, and the accumulated electrolyte states consist of cations ( $K^+$ ) from the solubilized salt and excess protons at the Stern layer that do not participate in the charge transfer process. These cations exist in a fully hydrated state in the bulk,<sup>52</sup> and the free energy change that occurs when these positively charged ions immobilize at the Stern layer involves a loss of entropy for these ions as well as a change in internal energy due to a partial loss of their hydration sphere. Their counterpart anions (such as  $H_2PO_4^-$  and  $HPO_4^{2-}$ ), on the other hand, merely lose some entropy when they enter the Stern phase, because they usually exist as dehydrated (or weakly solvated) molecules in the bulk.<sup>52</sup> Since the free energy change required to immobilize cations in the Stern layer is relatively larger, we expect that there are a greater number of protons that make up the electrolyte states in the Stern layer, which is reflected by the inequality in eq 34. Thus, the surface charge density in the Stern layer ( $\sigma_{Stern}$ ) at large cathodic potentials for these nanoscale thin film structures is created primarily by the interface reaction rather than by accumulation due to electrostatic forces. The functional form for  $\alpha$  in eq 33 shows that  $\alpha$  increases when  $C_{se}$  decreases or  $C_{sm}$  increases (or both), indicating that the metal–Stern layer coupling increases when there are a fewer number of accumulated electrolyte states or for a larger number of reactive states in the Stern layer. Since the system is not transport-limited,

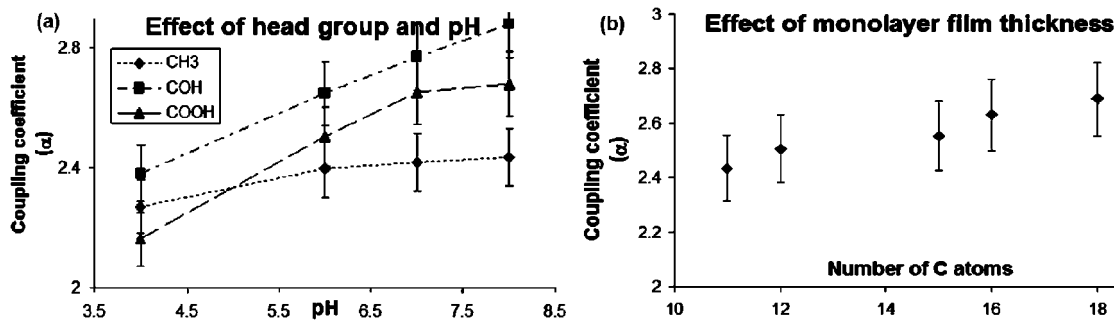


**Figure 10.** Coupling coefficient ( $\alpha$ ) values for diffusion-limited current as functions of (a) electrolyte pH and functional end group and (b) monolayer film thickness. For the experiments in part a, the monolayer film is 10 methylene units thick and the electrolyte is a 10 mM phosphate buffer solution. In part b, the alkane chains are all terminated by methyl functional groups and the electrolyte solution is a 10 mM phosphate buffer solution maintained at pH 8. The increase in the coupling coefficient in part b is larger than the null hypothesis by 1 standard deviation. Markers in part a are connected by dotted lines to clarify the graph.

increasing  $\beta$  also increases the value of  $\alpha$ , as can be seen from eq 33. However, the dependence of the coupling coefficient  $\alpha$  on monolayer thickness  $\beta$  is expected to be weak, since the thickness dependent term in eq 33 comes from the inclusion of the monolayer free charge density term  $\int_{-\beta}^0 \rho dx$  in eq 31. For applied potentials in which the finite charge size assumption<sup>26</sup> holds and the number of electrons in the monolayer film is limited by mutual Coulombic repulsion, the free charge density term is expected to be small in comparison to  $C_{sm}$  and  $C_{se}$ . We expect that the contribution due to the accumulated electrolyte states would be nearly the same for experimental systems with different functional end groups if the bulk electrolyte pH and concentration is kept constant. Thus, the primary reason for the increase in slope for more electronegative head groups is due to increased coupling of the monolayer–electrolyte interface with the metal due to a larger number of reactive electrolyte states (Figure 10a).

The relative magnitude of the coupling coefficient  $\alpha$  for different functional groups reveals some interesting details about the reaction at the monolayer–electrolyte interface. At lower pH, the metal–Stern layer coupling is weakest for a carboxyl-terminated monolayer chain and strongest for the hydroxyl functional group, whereas for higher bulk electrolyte pH, the deprotonation of the carboxylic group seems to considerably enhance the reaction between the reactive electrolyte states and the surface sites (Figure 10a). This suggests that the access of the reactive species in the Stern layer to electrons at the reactive surface sites ( $-\text{OH}$ ) of the carboxylic acid functional group is blocked by the double-bonded oxygen species ( $=\text{O}$ ) on the neighboring carboxylic functional group, as discussed before. The  $\text{sp}^3$  hybridized hydroxyl functional group, on the other hand, does not have these interfering  $\pi$  orbitals that can inhibit reactant access. In addition, the loss of the acidic proton at greater pH for the carboxylic functional group spreads the electronic charge over a set of delocalized orbitals in the functional group greatly, enhancing the available surface sites. The enhanced coupling between the metal phase and the electronegative functional groups is also an expected consequence of the increased chemical potential difference for an electron between the metal and the IHP, as discussed before, which causes an enhanced thermal diffusion of charge. In addition to these functional group specific effects, Figure 10a indicates that the values of  $\alpha$  increase with greater electrolyte pH for each headgroup because increasing electrolyte pH reduces the number of accumulated protonic electrolyte states in the Stern layer. However, the rate of increase in  $\alpha$  is steepest for the carboxylic acid functional group between pH values of 4 and 6, indicating an additional contribution due to an increasing number of reactive electrolyte states when the

functional group deprotonates. Thicker monolayer films also exhibit higher values of  $\alpha$ , as seen in Figure 10b, because of the length-dependent factor in eq 33, although the dependence on monolayer film thickness is weak, as discussed above. The parameter  $\alpha$ , like the Fowler–Nordheim potential energy barrier, is representative of an experimentally observed barrier to charge transfer, and this barrier is dependent on bulk electrolyte properties, even when the monolayer functional group and alkane backbone length are not varied. This functional dependence of  $\alpha$  on bulk electrolyte properties supports the underlying assumption that the main contribution to the charge transfer barrier is from the monolayer–electrolyte interface and any barrier at the gold–monolayer interface is unimportant.<sup>60</sup>

The net reduction current density does not exhibit any Fowler–Nordheim-like tunneling characteristics at large electric fields in the monolayer, as expected. For the electron at a monolayer surface site to tunnel through the barrier at the Stern layer, the electric field in the diffuse layer would have to distort the step potential energy barrier at the monolayer–electrolyte interface considerably in order that the zero-point energy of the electron in the electrolyte solution match closely with the energy of the electron in the surface site. However, since the maximum electric field in the diffuse layer is only  $10^4$  V/m, as demonstrated by the scaling arguments in the Supporting Information section, any such distortion in potential energy is vanishingly small. The absence of tunneling characteristics in the current density–electric field dependence for the large cathodic currents is further support that the dominant charge transfer barrier exists at the monolayer–electrolyte interface and not at the gold–monolayer interface. The energy barrier inhibiting charge transfer from the metal to the electrolyte is located at the gold–electrolyte interface when significant pinhole defects are present, as discussed before. The electric field calculated from the imaginary component of eq 1 would, in this case, describe the field acting in the pinhole structure. The magnitude of the distortion induced in the potential energy barrier at the gold–electrolyte interface in the pinhole by this field is comparable to the band bending for the anodic tunneling case described in the previous section ( $\sim 10^9$  V/m), yet there is no observable evidence of any tunneling mechanism in the current–electric field responses, indicating that a barrier at the gold–electrolyte interface, if present, is relatively insignificant compared to the charge transfer barrier at the monolayer–electrolyte interface.

**iv. Interface reaction-limited currents ( $V < V_{\text{PZF}}$ ).** For applied potentials that are slightly more cathodic (i.e.,  $V - V_{\text{PZF}} \sim -100$  mV) than the PZF, the computed electrostatic potential energy profile in the monolayer is qualitatively represented by

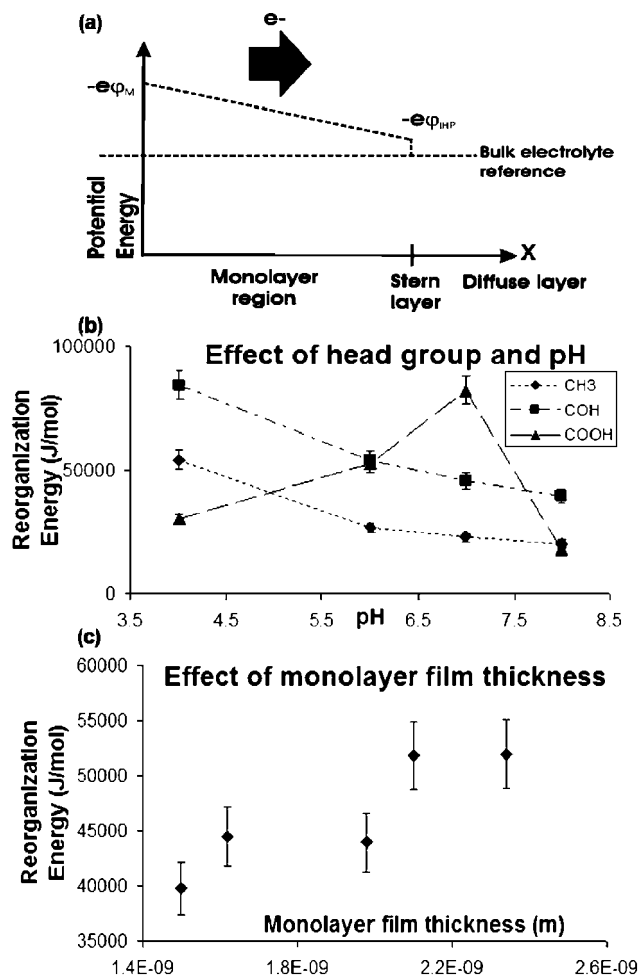


**Figure 11.** (a) Schematic illustrating the potential energy profile for applied potentials in the vicinity of the PZF. Reorganization energies as a function of (b) electrolyte pH and monolayer functional group and (c) monolayer film thickness. For the experiments in part b, the monolayer film is 10 methylene units thick and the electrolyte is a 10 mM phosphate buffer solution. In part c, the alkane chains are all terminated by methyl functional groups and the electrolyte solution is a 10 mM phosphate buffer solution maintained at pH 8. Markers in part b are connected by dotted lines to clarify the graph.

the schematic in Figure 11a, where the transferring electron experiences no potential energy barrier as it diffuses from the metal–monolayer interface to the monolayer–electrolyte interface. Instead, the observed current density is limited by the polarization free energy barrier that inhibits the chemical reaction between cationic electrolyte states occurring at the monolayer–electrolyte interface. Charge transfer between the reactants and the formation of the product species at the Stern layer occurs when an activated complex is formed, where the reaction system assumes a configuration of maximum free energy due to the stretching and compression of chemical bonds during collisions between the reacting species.<sup>65</sup> The rate-limiting step in the formation of an activated complex for the charge transfer reaction between the partially hydrated cationic species at the Stern layer and the monolayer functional group consists of the rearrangement of the solvent and reactant atomic polarizations from their equilibrium configurations.<sup>51</sup> This configuration rearrangement facilitates the adiabatic tunneling of the transferring electron from the electronic energy levels of the functional moiety to the corresponding isoelectronic energy level of the cationic species in the Stern layer.<sup>50</sup> This hypothesis presupposes that the Born–Oppenheimer approximation<sup>66–68</sup>

holds during the charge transfer process, which is a reasonable assumption given that there is no transport barrier inhibiting electron transport in the monolayer phase (Figure 2b), and there is also no electrostatic potential energy barrier at the monolayer–electrolyte interface that can limit the movement of the transferring electron. The current density is determined by the number of reactant–solvent complexes that overcome this atomic polarization reorganization energy barrier by thermal activation. Therefore, the observed current density depends on this activation free energy in an Arrhenius rate expression of the form

$$J \propto \exp\left(-\frac{\Delta G_R^*}{kT}\right) \quad (35a)$$

where

$$\Delta G_R^* = G^{\text{trans}} - G_R^0 = \frac{\lambda}{4} \left( \frac{e(\phi_M - E^0)}{\lambda} + 1 \right)^2 \quad (35b)$$

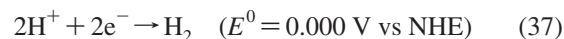
This expression for the difference between the free energy of the most probable activated complex configuration ( $G^{\text{trans}}$ )<sup>69</sup> and the free energy of the reactants in their standard states ( $G_R^0$ ) in eq 35b is the classic Marcus model<sup>70,71</sup> for the activation free energy in potential-dependent charge exchange between species. The term  $\lambda$  refers to the reorganization energy and can be expressed additively as the sum of internal ( $\lambda_i$ ) and external contributions ( $\lambda_o$ ). The internal reorganization energy refers to the contribution to the atomic polarization due to the changes in the bond length and bond angle within the internal coordination sphere of the reactant and product species. The external reorganization energy is representative of the change in the atomic polarization due to the nonequilibrium orientation of solvent molecules around the reacting electrolyte states.<sup>2,72</sup> The quantity  $E^0$  in eq 33 is the standard electrode potential for the reaction that is the primary contributor to the reduction current at the monolayer–electrolyte interface, and a comparison of the estimated values against tabulated standard reduction potentials helps identify the participating ionic species in the charge transfer reaction. These two experimental parameters, namely,  $\lambda$  and  $E^0$  can be calculated from the potential dependence of the observed current density as

$$\lambda = -\frac{e^2}{kT} \left( \frac{\partial^2(\ln J)}{\partial \phi_M^2} \right)^{-1} \quad (36a)$$

and

$$E^0 = \frac{\lambda}{e} \left( 1 + \frac{2kT}{e} \left( \frac{\partial(\ln J)}{\partial \phi_M} \right)_{\phi_M=0} \right) \quad (36b)$$

Note that the proportionality constant from eq 35a cancels in both differentiated terms in eqs 36a and 36b. The averaged value for  $E^0$  obtained from eq 36b, for all gold–monolayer–electrolyte systems, is  $-0.006 \pm 0.050$  V vs NHE, and this value corresponds to the theoretical standard reduction potential for protons in an aqueous solution<sup>6</sup> (reaction 37, below) within reasonable error, where



The values of  $\lambda$  for different functional groups at various bulk electrolyte pH conditions are depicted in Figure 11b. In comparing the  $-\text{CH}_3$  and  $-\text{COH}$  functional groups, we can see that the reorganization energy is larger for lower pH and for the hydrophilic end group ( $-\text{COH}$ ), indicating that larger energy changes accompany the rearrangements in the partial hydration

sphere of the reactant and product species as the number of cationic accumulated electrolyte states in the Stern layer increase and when the water repellency of the electrode surface decreases. As the number density of electrolyte states increases in the Stern layer, increased crowding inhibits changes in the solvation sphere of the participating ion, thereby increasing the energy required to polarize the outer solvent cage as the transition state is formed. Enhanced hydrophilicity at the electrode surface, on the other hand, increases the attraction between the aqueous solvent molecules of the partial hydration sphere of the protons at the Stern layer and the functional end group of the monolayer phase, thereby restricting the ability of the solvent molecules to reorganize around the reactant and product species. Thus, the formation of the transition state from the reactant or the product species in the vicinity of a hydrophilic  $-\text{COH}$  surface requires a larger energy input.

The results for  $\lambda$  in the case of the  $-\text{COOH}$  end group are vastly different as compared to the trends seen in the results discussed above, since the reorganization energy is observed to increase monotonically for  $\text{pH} < 7$  and subsequently decrease rapidly for  $\text{pH} > 7$  (Figure 11b). The abrupt change in this characteristic energy parameter indicates the existence of different mechanisms at work in the polarization reconfiguration rate-limiting step for the two pH regimes. For  $\text{pH} > 7$ , the carboxylic functional end group exists primarily in the deprotonated state, where the negative charge on the oxygen is delocalized over the resonance stabilized structure that characterizes the acidic moiety, as discussed before. The semihydrated proton at the Stern layer experiences no steric barrier in accessing the active site, and therefore, the estimated reorganization energy in this pH range is simply representative of the rearrangement of the solvent configuration around the proton, which is easier at higher pH when there is less crowding due to other protons at the Stern layer. The negative charge on the functional group also facilitates a favorable Coulombic interaction with the positively charged cationic species that reduces the distance of closest approach between the electrolyte states and the functional end group. As a consequence, the tunneling barrier in the activated complex for the transferring electron decreases, and this, in turn, reduces the amount of reorganization required in the electron donor and acceptor polarizations to make the electron energy levels in both species equal. This hypothesis explains the decrease in reorganization energies for  $\text{pH} > 7$ . For pH values less than 7, the access of the proton to the surface site ( $-\text{OH}$ ) on the functional end group is blocked by the  $\text{sp}^2$  orbitals of the  $\text{C}=\text{O}$  bond. Thus, the change in the atomic polarization that facilitates the charge exchange step involves a rotation of the carboxylic species around the sigma  $\text{C}-\text{C}$  bond that tethers the functional group to the alkane chain such that the hydroxyl moiety on the carboxylic functional group is now exposed to the electrolyte states at the Stern layer. The rate-limiting step, although still a reconfiguration in the atomic polarization, involves the functional end group and not the partially hydrated electron-accepting species in the Stern layer. This rotation would expose the lone pairs of electrons on the oxygen of the  $-\text{OH}$  group to the electrolyte, and so increasing the concentration of negative hydroxyl species in the electrolyte by increasing the pH makes the rotation step more energetically unfavorable, which is seen by the increase in the reorganization energy. As the pH increases to values greater than the surface  $\text{pK}_a$ , the rotation step becomes less important for the charge transfer reaction, since most of the surface sites exist as the deprotonated delocalized electron donors. This transition, from functional group reorganization being rate-limiting to solvent

reorganization around the cationic electrolyte state being rate-limiting, is manifested by the abrupt change in the dependence of the  $\lambda$  parameter on electrolyte pH.

The contribution of the monolayer thickness to the reorganization energy is depicted in Figure 11c. Since the  $\lambda$  values are compared for identical bulk electrolyte conditions, the conditions affecting the polarization rearrangement due to crowding at the Stern layer are kept constant. Therefore, the increase in the reorganization energy with increased monolayer thickness can be attributed to a reduced interaction between the monolayer functional group ( $-\text{CH}_3$ ) and the cationic electrolyte states. This reduced interaction arises due to an increased spacing between the electronic charge density in the metal and the positively charged protons at the Stern layer for thicker monolayer films. Oscillations in the values of the reorganization energy due to differences in the packing of even- and odd-numbered carbon units in the alkane chain are observed here. This dependence of reorganization energy on the number of methylene groups in the monolayer phase has also been observed in gold-monolayer-electrolyte systems in which the redox molecule is tethered to the alkane phase as the functional end group.<sup>22</sup>

## Conclusion

We present an overview of the potential dependent charge transport characteristics of a monolayer modified gold electrode for the specific case in which the electrolyte does not contain any redox-active ion. The current-potential behavior in a gold-monolayer-electrolyte system is limited by the largest barrier to electron transfer within the system. We hypothesized the existence of three possible energy barriers; namely, the electrostatic potential energy barriers at the gold-monolayer and at monolayer-electrolyte interfaces, as well as a transport barrier within the monolayer phase. We also provided a semiquantitative justification to demonstrate that the electrostatic potential barrier to charge exchange at the gold-monolayer interface, for a pinhole-free monolayer, is relatively insignificant compared to the other two barriers. The phase of the low-frequency impedance data is demonstrated to be a qualitative indicator of the nature of the barrier that inhibits the charge exchange process, in which a small deviation from an ideal capacitive behavior indicates that charge transport through the monolayer phase is rate-limiting. On the other hand, a purely resistive response is indicative of charge transfer at an interface as being the rate-limiting mechanism. For a defect-free monolayer, this charge transfer barrier corresponds to the monolayer-electrolyte potential energy barrier. Several observations are made throughout the paper to support our hypothesis that the charge transfer barrier at the gold-monolayer interface is relatively insignificant compared to the barrier at the monolayer/electrolyte interface.

An analytical technique that utilizes the constitutive charge transport equation in a modified form to fit the low frequency impedance data for a gold-monolayer-electrolyte system enables the evaluation of the conduction and diffusion components of the net current density for different potential regimes. For applied potentials that are anodic of the PZF, the electric field driven drift of electrons through the monolayer phase is the main contributor to the observed oxidation current density. This anodic conduction current within the monolayer is observed to transition from Ohmic conduction to space-charge-limited current at higher electric fields. These conduction mechanisms are postulated from the current-potential behavior without presupposing a transport model for the moving charge and are

in keeping with the observed low frequency impedance response that indicates that charge transport through the monolayer phase limits the charge exchange process for this potential regime. For larger anodic potentials, the impedance response acquires a small but significant real component, and the net current density demonstrates characteristics associated with Fowler–Nordheim tunneling in which the electron quantum mechanically penetrates a potential energy barrier that separates the ground energy level of the participating anion from corresponding empty states in the metal. This potential energy barrier depends on the chemical potential of the electron-donating anionic species at the Stern layer and on the electronegativity of the monolayer functional group. Therefore, the tunneling barrier is sensitive to bulk electrolyte properties that can affect the ground-state energy levels of the anionic species as well as to the properties of the monolayer functional group at the IHP.

For potentials that are sufficiently more cathodic than the PZF, we demonstrate that the diffusion current contributes primarily to the observed reduction current density and the functional dependence of the diffusion current on the applied potential displays characteristics of thermally activated electron emission over an energy barrier. Thus, we hypothesize that the response of the gold–monolayer–electrolyte system to applied potential for the cathodic potential regime is no longer limited by the rate of electron transport through the monolayer, but rather, by the rate of electron transfer between the surface sites at the monolayer functional groups and the participating cations in the Stern layer.

We also developed a model for charge transfer at the monolayer–electrolyte interface based on thermionic emission theory that provides a quantitative estimate for the extent of coupling between the metal and the Stern layer and between the Stern layer and the bulk electrolyte solution. The model indicates that at large cathodic potentials, the electronic coupling between the metal and the reacting electrolyte states is stronger than the coupling between these states and the bulk electrolyte. We also showed that the tuning of bulk electrolyte conditions and the chemistry of the functional group can have a significant impact on the relative importance of the two kinds of coupling. The charge transfer process for applied potentials within the vicinity of the PZF, however, is limited by the free energy barrier to the rearrangement of the atomic polarization of the monolayer functional group at the IHP and the partially hydrated cationic species at the OHP. The functional dependence of the current on applied potential within this voltage regime is also fit to the classic Marcus relation to compute the reorganization energy and standard electrode reduction potential for the charge transfer reaction.

The application of this analytical technique to the low-frequency impedance response of ordinary gold–monolayer–electrolyte systems yields a significant amount of detail from which the structure and properties of the monolayer–electrolyte interface can be constructed. Thus, the monolayer on gold system complemented with the detailed analysis outlined in this paper can prove to be a powerful platform for the detection and quantification of various electrostatic and steric interactions between the ions, solvent molecules, and the monolayer functional groups.

**Acknowledgment.** This work was performed within Nano-CEMMS; University of Illinois Nano-Science and Engineering Center (NSEC), supported by the National Science Foundation under Award No. DMI-0328162.

**Supporting Information Available:** This information is available free of charge via the Internet at <http://pubs.acs.org>.

## Appendix

### Glossary

$\alpha$	coupling coefficient
$\beta$	monolayer film thickness
$C_{se}$	capacitance/unit area of accumulated cations at Stern layer
$C_{sm}$	capacitance/unit area of reactive cations at Stern layer
$D$	diffusivity of charge carrier in monolayer
$e$	electronic charge
$E$	electric field in monolayer
$E^0$	standard redox potential for reduction reaction at monolayer–electrolyte interface
$E_{tunn}$	characteristic electric field describing onset of tunneling
$\bar{E}_{micro}^P(x)$	microscopic electric field in phase P (P = monolayer, metal, Stern layer)
$\bar{E}(x)$	averaged macroscopic electric field
$\bar{E}^{near}(x)$	microscopic contribution to the electric field from immediate neighborhood
$\bar{E}_{macro}^{near}(x)$	macroscopic contribution to the electric field from immediate neighborhood
$\epsilon_d$	static dielectric permittivity of diffuse layer
$\epsilon_M$	static dielectric permittivity of monolayer
$\epsilon_0$	dielectric permittivity of vacuum
$\epsilon_t$	total electron energy
$\epsilon'$	electron energy perpendicular to monolayer–electrolyte interface
$\epsilon_0'$	electron energy at the Fermi level of an NHE measured with respect to vacuum
$F_f$	occupation probability for energy states of anion in electrolyte
$F_e$	Fermi–Dirac probability that electron state in metal is empty
$G^{trans}$	free energy of most probable activated transition complex
$G_R^0$	free energy of reactants at standard conditions
$\Delta G_R^*$	free energy barrier for reduction reaction
$\hbar$	modified Planck's constant
$J_{cond}$	average conduction current density
$J_{diff}$	average diffusion current density
$J_{FN}$	tunneling current density
$J_{SLC}$	space–charge-limited current density
$J_{total}, J$	Average direct current density
$k$	Boltzmann constant
$\kappa$	fraction of space charge from diffusion-injected electrons
$L$	penetration length
$\lambda$	reorganization energy
$m_e$	free electron mass
$m^*$	effective electron mass
$\mu$	mobility of charge carriers in monolayer
$n(\epsilon_t)$	number density of electrons with energy $\epsilon_t$
$n_{Ohmic}$	number density of charge carriers in Ohmic regime
$N_f$	density of occupied energy states of an anion at the Stern layer
$v_x$	velocity of electrons in $x$ direction
$P(\epsilon')$	probability that electron with perpendicular energy $\epsilon'$ can penetrate energy barrier at monolayer–electrolyte interface

$\bar{P}_M(x)$	local polarization density in the monolayer induced by surface charge at the metal–monolayer interface
$\bar{P}_E(x)$	local polarization density in the monolayer induced by surface charge at the monolayer–electrolyte interface
$\rho$	free charge density in monolayer
$\rho_{\text{Ohmic}}$	free charge density in monolayer in the Ohmic regime
$\sigma_{\text{cond}}$	average monolayer conductivity
$\sigma_M$	surface charge density at metal–monolayer interface
$\sigma_{\text{Stern}}$	surface charge density at monolayer–electrolyte interface
$T$	temperature
$\varphi_M$	potential at metal–monolayer plane
$\varphi_{\text{IHP}}$	potential at IHP
$\varphi_{\text{OHP}}$	potential at OHP
$\Delta\varphi_i$	potential drop across monolayer
$\Delta\varphi_{\text{Stern}}$	potential drop across Stern layer
$\Phi$	tunneling potential energy barrier
$\omega$	angular frequency
$V_0$	minimum velocity required by electron to cross potential energy barrier at IHP
$Y_{\text{sys}}$	admittance of gold–monolayer–electrolyte system
$Y_{\text{sys}}^{\text{Re}}$	real component of system admittance
$Y_{\text{sys}}^{\text{Im}}$	imaginary component of system admittance

## References and Notes

- Chidsey, C. E. *Science* **1991**, *251*, 919.
- Bard, A. J.; Abruna, H. J.; Chidsey, C. E.; Faulkner, L. R.; Feldberg, S. W.; Itaya, K.; Majda, M.; Melroy, O.; Murray, R. W.; Soriaga, M. P.; White, H. S. *J. Phys. Chem.* **1993**, *97*, 7147.
- Finklea, H. O.; Hanshaw, D. D. *J. Am. Chem. Soc.* **1991**, *114*, 3173–3181.
- Finklea, H. O.; Ravenscroft, M. E.; Snider, D. A. *Langmuir* **1993**, *9*, 223.
- Acevedo, D.; Abruna, H. D. *J. Phys. Chem.* **1991**, *95*, 9590.
- Bard, A. J.; Faulkner, L. R. *Electrochemical Methods: Fundamentals and Applications*; John Wiley & Sons, Inc.: New York, 2001.
- Miller, C.; Cuendet, P.; Gratzel, M. *J. Phys. Chem.* **1991**, *95*, 877.
- Becka, A.; Miller, C. *J. Phys. Chem.* **1992**, *96*, 2657.
- Smalley, J. F.; Finklea, H. O.; Chidsey, C. E. D.; Linford, M. R.; Creager, S. E.; Ferraris, J. P.; Chalfant, K.; Zawodzinski, T.; Feldberg, S. W.; Newton, M. D. *J. Am. Chem. Soc.* **2003**, *125*, 2004.
- Finklea, H. O. *J. Phys. Chem. B* **2001**, *105*, 8685.
- Lyons, M. E. G. *Sensors* **2002**, *2*, 314.
- Newton, M. D.; Smalley, J. F. *Phys. Chem. Chem. Phys.* **2007**, *9*, 555.
- Liu, B.; Bard, A. J.; Mirkin, M. V.; Creager, S. E. *J. Am. Chem. Soc.* **2004**, *126*, 1485.
- Schmickler, W. *J. Electroanal. Chem.* **1977**, *83*, 387.
- Schmickler, W. *J. Electroanal. Chem.* **1977**, *82*, 65.
- Finklea, H. O.; Hanshaw, D. D. *J. Am. Chem. Soc.* **1991**, *114*, 3173.
- Adams, D. M.; Brus, L.; Chidsey, C. E.; Creager, S. E.; Creutz, C.; Kagan, C. R.; Kamat, P. V.; Lieberman, M.; Lindsay, S.; Marcus, R. A.; Metzger, R. M.; Michel-Beyerle, M. E.; Miller, J. R.; Newton, M. D.; Rolison, D. R.; Sankey, O.; Schanze, K. S.; Yardley, J.; Zhu, X. *J. Phys. Chem. B* **2003**, *107*, 6668.
- Gosavi, S.; Marcus, R. A. *J. Phys. Chem. B* **2000**, *104*, 2067.
- Newton, M. D. *Chem. Rev.* **1991**, *91*, 767.
- Newton, M. D.; Sutin, N. *Annu. Rev. Phys. Chem.* **1984**, *35*, 437.
- Slowinski, K.; Chamberlain, R. V.; Miller, C. J.; Majda, M. *J. Am. Chem. Soc.* **1997**, *119*, 11910.
- Smalley, J. F.; Feldberg, S. W.; Chidsey, C. E.; Linford, M. R.; Newton, M. D.; Liu, Y. *J. Phys. Chem.* **1995**, *99*, 13141.
- Schweiss, R.; Werner, C.; Knoll, W. *J. Electroanal. Chem.* **2003**, *540*, 145.
- Boubour, E.; Lennox, R. B. *J. Phys. Chem. B* **2000**, *104*, 9004.
- Boubour, E.; Lennox, R. B. *Langmuir* **2000**, *16*, 4222.
- Gupta, C.; Shannon, M. A.; Kenis, P. J. A. *J. Phys. Chem. C* **2008**, *xx*, submitted.
- Burgess, I.; Seivewright, B.; Lennox, R. B. *Langmuir* **2006**, *22*, 4420.
- Komura, T.; Yamaguchi, T.; Shimatani, H.; Okushio, R. *Electrochim. Acta* **2004**, *49*, 597.
- Creager, S. E.; Wooster, T. T. *Anal. Chem.* **1998**, *70*, 4257.
- Komura, T.; Yamaguchi, T.; Takahashi, K.; Terasawa, H. *J. Electroanal. Chem.* **2000**, *481*, 183.
- Molinero, V.; Calvo, E. J. *J. Electroanal. Chem.* **1998**, *445*, 17.
- Boubour, E.; Lennox, R. B. *Langmuir* **2000**, *16*, 7464.
- Love, J. C.; Estroff, L. A.; Kriebel, J. K.; Nuzzo, R. G.; Whitesides, G. M. *Chem. Rev.* **2005**, *105*, 1103.
- Ashcroft, N. W.; Mermin, D. W. *Solid State Physics*, College ed.; Thomson Learning: New York, 1976; p 826.
- Russakov, G. *Am. J. Phys.* **1970**, *38*, 1188.
- Jackson, J. D. *Classical Electrodynamics*; John Wiley: New York, 1998; p 809.
- Stoner, C. E. *Philos. Mag.* **1945**, *36*, 803.
- Laibinis, P. E.; Whitesides, G. M.; Allara, D. L.; Tao, Y.; Parikh, A. N.; Nuzzo, R. G. *J. Am. Chem. Soc.* **1991**, *113*, 7152.
- Nuzzo, R. G.; Dubois, L. H.; Allara, D. L. *J. Am. Chem. Soc.* **1990**, *112*, 558.
- Rose, A. *Phys. Rev.* **1955**, *97*, 1538.
- O'Dwyer, J. J. *J. Appl. Phys.* **1966**, *37*, 599.
- Lampert, M. A.; Mark, P. *Current Injection in Solids*, 1st ed.; Academic Press Inc.: New York, 1970; p 350.
- Sze, S. M.; Kwok, K. N. *Physics of Semiconductor Devices*; Wiley-Interscience: New York, 2006; p 815.
- Fowler, R. H.; Nordheim, L. *Proc. R. Soc. London, Ser. A* **1928**, *119*, 173.
- Stern, T. E.; Gossling, B. S.; Fowler, R. H. *Proc. R. Soc. London, Ser. A* **1929**, *124*, 699.
- Bardeen, J. *Phys. Rev. Lett.* **1960**, *6*, 57.
- Esaki, L. *Rev. Mod. Phys.* **1974**, *46*, 237.
- Jensen, K. L. *J. Vac. Sci. Technol., B* **2003**, *21*, 1528.
- Young, R. D. *Phys. Rev.* **1959**, *113*, 110.
- Levich, V. G. *Adv. Electrochem. Electrochem. Eng.* **1966**, *4*, 249.
- Marcus, R. A. *J. Chem. Phys.* **1956**, *24*, 966.
- Bernal, J. D.; Fowler, R. H. *J. Chem. Phys.* **1933**, *1*, 515.
- Bockris, J. O. M.; Reddy, A. K. N.; Gamboa-Aldeco, M. *Modern Electrochemistry 2A: Fundamentals of Electrode Processes*, 2nd ed.; Plenum: New York, 2000; Vol. 2A, p 771–1529.
- Gurney, R. W. *Proc. R. Soc. London, Ser. A* **1931**, *134*, 137.
- Kittel, C.; Kroemer, H. *Thermal Physics*, 2nd ed.; W. H. Freeman: New York, 1980; p 496.
- Boulas, C.; Davidovits, J. V.; Rondelez, F.; Vuillaume, D. *Phys. Rev. Lett.* **1996**, *76*, 4797.
- Kakiuchi, T.; Iida, M.; Imabayashi, S.; Niki, K. *Langmuir* **2000**, *16*, 5397.
- Dai, Z.; Ju, H. *Phys. Chem. Chem. Phys.* **2001**, *3*, 3769.
- Campbell, I. H.; Rubin, S.; Zawodzinski, T. A.; Kress, J. D.; Martin, R. L.; Smith, D. L.; Barashkov, N. N.; Ferraris, J. P. *Phys. Rev. B* **1996**, *54*, 14321.
- Parker, I. D. *J. Appl. Phys.* **1993**, *75*, 1656.
- Card, H. C.; Rhoderick, E. H. *J. Phys. D: Appl. Phys.* **1971**, *4*, 1589.
- Chang, C. Y.; Sze, S. M. *Solid-State Electron.* **1970**, *13*, 727.
- Crowell, C. R.; Sze, S. M. *Solid-State Electron.* **1966**, *9*, 1035.
- Card, H. C. In *Tunneling MIS Structures*, Institute of Physics Conference Series, 1980, p 140.
- Eyring, H. *J. Chem. Phys.* **1935**, *3*, 107.
- Griffiths, D. J. *Introduction to Quantum Mechanics*, 2nd ed.; Benjamin Cummings: New York, 2004; p 480.
- Kuznetsov, A. M.; Ulstrup, J. *Electron Transfer in Chemistry and Biology: An Introduction to Theory*; 1st ed.; John Wiley & Sons: New York, 1999; p 356.
- Pauling, L.; Wilson, E. B. *Introduction to Quantum Mechanics with Applications to Chemistry*; reprint ed.; Dover: New York, 1985; p 468.
- Marcus, R. A. *J. Chem. Phys.* **1956**, *24*, 979.
- Marcus, R. A. Office of Naval Research: 1957; Project No. 051-331.
- Marcus, R. A. *J. Chem. Phys.* **1965**, *43*, 679.
- Marcus, R. A. *Annu. Rev. Phys. Chem.* **1964**, *15*, 155.